Publisher: Springer
Journal: Journal of Mathematical Biology
Publisher version: https://doi.org/10.1007/s00285-016-1087-0

Demyelination Patterns in a Mathematical Model of Multiple Sclerosis

M.C. Lombardo · R. Barresi · E. Bilotta · F. Gargano · P. Pantano · M. Sammartino

Abstract In this paper we derive a reaction-diffusion-chemotaxis model for the dynamics of Multiple Sclerosis. We focus on the early inflammatory phase of the disease characterized by activated local microglia, with the recruitment of a systemically activated immune response, and by oligodendrocyte apoptosis. The model consists of three equations describing the evolution of macrophages, cytokine and apoptotic oligodendrocytes. The main driving mechanism is the chemotactic motion of macrophages in response to a chemical gradient provided by the cytokines. Our model generalizes the system proposed by Calvez and Khonsari in [15, 48] to describe Baló sclerosis, a rare and aggressive form of multiple sclerosis. We use a combination of analytical and numerical approaches to show the formation of different demyelinating patterns. In particular, a Turing instability analysis demonstrates the existence of a threshold value for the chemotactic coefficient above which stationary structures develop. In the case of subcritical transition to the patterned state, the numerical investigations performed on a 1-dimensional domain show the existence, far from the bifurcation, of complex spatio-temporal dynamics coexisting with the Turing pattern. On a 2-dimensional domain the proposed model supports the emergence of different demyelination patterns: localized areas of apoptotic oligodendrocytes, which closely fit existing MRI findings on the active MS lesion during acute relapses; concentric rings, typical of Baló sclerosis; small clusters of activated microglia in absence of oligodendrocytes apoptosis, observed in the pathology of preactive lesions.

Keywords Multiple Sclerosis · Inflammation · Chemotaxis PDE model · Turing instability · Patterns

Mathematics Subject Classification (2010) 92C15 · 92C17 · 92C37 · 92C40

1 Introduction

Multiple Sclerosis (MS) pathology is a debilitating and progressive autoimmune disease primarily expressed as multiple focal areas of myelin loss in the white matter of the brain called plaques or lesions. Myelin is a substance produced by oligodendrocytes that provides the protective coating around nerve fibers in the Central Nervous System (CNS) to help transmission of nerve impulses and it is a primary objective of the immune attack in MS. The body's immune system of MS patients produces an inflammatory state which destroys the oligodendrocytes and the myelin sheath around nerves (demyelination process) and causes an axonal damage of the central nervous system.

The pathological analysis of actively demyelinating lesions has revealed a profound heterogeneity between disease stages and between individual patients, suggesting that a variety of fundamentally different immunological mechanisms involving cytotoxic T-cells, B-cells, auto-antibodies and activated macrophages or microglia, likely come into play, maybe acting in parallel. Four major types of demyelinations, staged according to demyelinating activity, have been recently classified, suggesting different targets of injury and mechanisms of demyelination in each subtype [62]. Around 50% of patients displays type II lesions, characterized by the presence of immunoglobulin and complement deposit and abundance of remyelinating shadow plaques. The remaining lesions are distributed between type I (15% of patiens), an immune-type pattern with high incidence of remyelinating plaques and absence of complement deposition on a backgound of activated

This work has been partially supported by the GNFM-INDAM.

M.C. Lombardo · R. Barresi
Department of Mathematics, University of Palermo, Italy.
E-mail: {mariacarmela.lombardo} {rachele.barresi} @unipa.it

F. Gargano · M. Sammartino
Department of Engineering, University of Palermo,Italy.
E-mail: {francesco.gargano} {marcomarialuigi.sammartino}@unipa.it

E. Bilotta · P. Pantano
Department of Physics, University of Calabria, Italy.
E-mail: {eleonora.bilotta} {pietro.pantano} @unical.it

microglia inflammatory background, and type III lesions (about 30% of patiens), exhibiting extensive zones of apoptotic oligodendrocytes and microglial activation in a myelinated tissue with few or no T-lymphocytes, no evidence of complement activation, and no remyelinating shadow plaques. Type IV lesions (only about 1% of patients) are extremely rare and show dying non-apoptotic oligodendrocytes in the periplaque white matter, probably due to a potential primary metabolic oligodendrocyte disfunction. In the reported cases, neither overlap in pattern nor a change between different lesion types was observed during the clinical course of individual patients (intra-individual homogeneity). Myelin is considered to be the primary target of the inflammatory response in the type II lesions, whereas type III lesions are thought to reflect primary oligodendrocyte injury.

These findings would lead to two different mechanisms of demyelination: in type I and II microglial activation is mediated by adaptive immunity characterized by a T-cell dependent, macrophage-mediated, autoimmune attack on constituents in the normal myelin sheath, while in type III lesions demyelination would be provoked by innate immunity activated processes which have been recently found to be able to activate microglia [66]. An alternative hypothesis has been proposed by Barnett and Prineas [2, 3], based on the analysis of the pathological events preceding myelin phagocytosis ('pre-demyelinating' lesions) in patients with fulminant MS deceased shortly after a relapse. They observed hypoxia-like lesions, characterized by extensive oligodendrocyte apoptosis on a background of early microglial activation but few or no infiltrating lymphocytes or myelin phagocytes (type III lesions). Moreover they found the presence of two different lesion types (type II and III) within one patient, consistent with intra-individual heterogeneity, or stage-dependent pathology. On the basis of these results, the authors suggest that the pathological heterogeneity observed in MS could largely be due to evolution of lesional pathology, rather than pathogenic heterogeneity: namely, type III lesions would represent a very early stage in the formation of most, if not all, MS lesions which would then evolve towards the second T-cell-mediated stage of the disease. The paradigm of a stage-dependent disease has been recently confirmed by the study of Breij et al. [12].

However to date the debate whether MS is a interindivual heterogeneous 1-stage disease or the pathogenic dynamics can change during the clinical course is still unresolved and the question on what mechanism underlies different lesion types remains unanswered.

In this paper we introduce a continuous model of MS which aims to reproduce the initial stages of the demyelination process through oligodendrocyte destruction driven by activated macrophages. This corresponds to type III lesions in the scenario of interindividual heterogeneity-intraindividual homogeneity proposed by Lucchinetti et al. [62] or to the 'pre-demyelinatig' phase of the disease in the paradigm hypothesized by Barnett and Prineas. We want to investigate the formation of plaques of demyelinated areas on 2D sections of the white matter, which are the characteristic neuropathological lesions of multiple sclerosis [55].

Inflammation is a major hallmark of multiple sclerosis pathology and the experimental data suggest that macrophages activation is driven by inflammation throughout all stages of the disease: in the early stages (the so-called Relapsing-Remitting phase), the process is characterized by inflammation-driven focal demyelinating lesions associated with massive activated microglia and infiltrated macrophages. With the progression of the disease (in patients with primary or secondary progressive MS) the inflammatory response may decrease and becomes trapped behind a repaired blood brain barrier. In any case, active demyelination and neurodegeneration are invariably associated with inflammation [58], which is recognized as the major driver of clinical disease and tissue injury [91]. In our model we shall describe the chemosensitive motion of activated microglia using a modification of the classical Keller-Seger model of chemotaxis, that has been proposed to describe the aggregation phase in a variety of different biological phenomena in which the main role is played by cellular self organization. Chemotactic signaling and motility of macrophages is also assumed in the few mathematical models of acute inflammatory processes which take into account spatial variations [17, 26, 60, 77, 81]. We move from the model proposed by Khonsari and Calvez [48], who introduced a chemotaxis system based on partial differential equations to elucidate the dynamic processes involved in the so called Baló's sclerosis, a rare form of multiple sclerosis characterized by concentric demyelination areas. With respect to the Khonsari-Calvez model we present some modifications: we choose a different analytical form for the chemotactic sensitivity function, which still displays saturation at high cells densities to prevent solutions blow-up, but does not degenerate close to the stable homogeneous equilibrium. We also consider a different dynamics for the pro-inflammatory cytokines, removing the quasi-steady state approximation considered in [48] and allowing for an evolutive equation whose characteristic time scale can be varied to investigate its effects on the corresponding solutions. Finally, we introduce in the local equation for the pro-inflammatory cytokines a linear production term from the activated microglia, which are the principal source of chemical mediators driving inflammatory demyelination in MS [10]. Therefore this term accounts for the release of cytotoxic factors by 'classically activated' M1 microglia under pathological conditions [76]. We shall show that the presence of linear degradation and production by macrophages in the cytokine kinetics is able to induce the appearance of concentric rings. In fact, a key hypothesis in the Khonsari-Calvez model to describe the

formation of the ring structures is that the chemical signals attracting the macrophages are produced by the destroyed oligodendrocytes which, locally recruiting the surrounding macrophages, protect the neighbouring myelin sites from being attacked. Therefore in the model proposed in [48] the pro-inflammatory cytokines are produced by the damaged olygodendrocytes through a first order kinetic term and no cytokine production from macrophages is considered. On the other hand we shall see that the model presented in this paper supports the formation of concentric rings also in absence of oligodendrocyte-driven cytokine production. We postpone to Section 7 a comparison between the Khonsari-Calvez model and the model presented here, where the different assumptions and results are highlighted.

Through both Turing stability analysis and numerical simulations we perform a detailed investigation of the effects produced by variation of the system parameters on the relevant characteristics of the emerging aggregates, such as form, size and spacing. The aim of the present analysis is to show that the proposed model, within the experimentally available numerical values of the parameters, is able to predict the appearance of aggregates that qualitatively reproduce some of the patterns of demyelinated lesions typical of multiple sclerosis.

We have tested the dynamical behaviors of the proposed system starting our analysis on a one dimensional domain. In this case the analytic and numerical investigations performed yielded the conditions for the appearance of stationary non constant solutions and provided evidence for the occurrence of more complicated patterns, such as oscillatory and irregular spatio-temporal dynamics. In the more realistic case of a 2D domain, we have investigated the phenomenon of formation of the plaques close to the Turing instability threshold, carrying out a detailed sensitivity analysis aimed to probe the effect of varying the parameters on the plaques.

The paper is organized as follows: in Section 2 we introduce the model and the relevant parameters, and briefly account for the mathematical literature on chemotaxis-related systems. In Section 3 we perform a Turing stability analysis close to the stable homogeneous equilibrium which yields the critical value of the chemotactic coefficient above which spatial pattern are observed. Moreover the critical wavenumber of the resulting structures is found. In Section 4 the parameter values adopted in the analysis are specified, either taken from experimental literature or estimated. In Section 5 a detailed investigation of the system dynamics on 1D domains is performed: a weakly nonlinear analysis close to the Turing instability threshold is carried out and numerical bifurcation diagrams are shown that provide useful insight out of equilibrium. Section 6 provides the numerical simulations performed on 2D domains together with a detailed analysis on the effects produced by variations of the parameters affecting the characterization of the demyelinated plaques. In Section 7 we compare the hypotheses and results of the present system with the Khonsari-Calvez model. Finally in Section 8 some conclusions are drawn and perspectives for future work given.

2 Model description

The focus of this paper is the description of the initial stage of the disease (or type III lesions). As already discussed in the Introduction, this phase is characterized by macrophages and activated microglia, which dominate the inflammatory reaction triggering the production of a cocktail of pro-inflammatory cytokines [28]. In addition early lesions present areas of extensive oligodendrocyte apoptosis with a low grade of lymphocyte infiltration.

Therefore we shall propose a model which describes the spatio-temporal dynamics of the following three species:

$\tilde{m}(T,\mathbf{X})$ the density of activated macrophages,

$\tilde{c}(T,\mathbf{X})$ the concentration of chemoattractants and

$\tilde{d}(T,\mathbf{X})$ the density of the destroyed oligodendrocytes.

All the concentrations depend on time, T, and on the position, $\mathbf{X}$, where $(T,\mathbf{X}) \in \mathbb{R}^+ \times \Omega$, and Ω is a bounded domain, $\Omega \subset \mathbb{R}^n$, $n = 1,2$.

Since we are interested in the description of self-aggregating phenomena, we shall impose no-flux (homogenous von Neumann) boundary conditions.

2.1 Activated macrophages $\tilde{m}(T,\mathbf{X})$

The evolution of the density of activated macrophages/microglia is ruled by the following equation:

$$\frac{\partial \tilde{m}}{\partial T} = \underbrace{D\Delta_{\mathbf{X}}\tilde{m}}_{\text{Diffusion}} + \underbrace{\lambda\tilde{m}(\bar{m}-\tilde{m})}_{\text{Production/Decay}} \underbrace{-\nabla_{\mathbf{X}}\cdot(\Psi(\tilde{m})\nabla_{\mathbf{X}}\tilde{c})}_{\text{Chemotaxis}}, \qquad \text{with} \quad \Psi(\tilde{m}) = \psi\frac{\tilde{m}}{\bar{m}+\tilde{m}}. \tag{1}$$

The first term on the right hand side of Eq.(1) describes the random movement of the activated macrophages, where $\nabla_{\mathbf{X}} = \partial/\partial\mathbf{X}$, $\Delta_{\mathbf{X}} = \nabla_{\mathbf{X}} \cdot \nabla_{\mathbf{X}}$ and D is the diffusion constant. The next term describes the production and saturation of the activated macrophages: it is in fact hypothesized that activation of microglia may be responsible for the appearance of early MS lesions [79] but the underlying mechanism still remains unknown. Namely, in type II lesions it could be produced by activated T-lymphocytes, while in type III lesions macrophage activation is pronounced on a background of rather mild T-cells infiltration [2, 66]. This suggests that other mechanisms mediated by innate-immunity, for example through signaling via toll-like receptor, could take place [66]. So if, from the one hand, autoimmunity against CNS antigens is one possible explanation for macrophages activation [42], another possible mechanism could be that a persistent infection (like the Epstein–Barr virus [57]) triggers an immunopathological response either directly or through autoimmunity. However, despite of the intensive search for the target antigens of MS, no study has yet led to unequivocal identification of the antigen nor a generally accepted explanation of the activation mechanism has been provided. Here we do not try to represent the activation process and describe the dynamics only of those macrophages which are already transformed in an autoimmune active state. We just assume that an activation front travels in the white matter and drives the macrophages into their active state. This is supported by the clinical evidence that activated microglia in MS patients are found outside the histopathologically defined borders of multiple sclerosis plaques and in areas, such as the cerebral central grey matter, that are not normally reported as sites of pathology [1] and by the observation of the existence of an activation gradient of microglia from the periplaque white matter into the active plaques [53, 56]. Therefore we describe the rate of macrophages activation choosing a logistic functional form which takes into account the proliferation and saturation effects that have been also described in ODE models of acute inflammation [52, 82]. Here λ is the production rate of activated macrophages and $\bar{m}$ is the characteristic density of macrophages, i.e. the mean value of their initial distribution in the white matter of the brain. The third term on the right hand side describes chemotactic motion of activated macrophages in response to the gradient of the chemoattractant density $\tilde{c}(T, \mathbf{X})$. In fact, because of their ability to migrate to sites of tissue infection, activated macrophages are attracted by the cytokine signal, responding to a chemical stimulus and moving up the chemical gradient. We adopt a modified version of the Keller-Segel equations, the so-called cell-kinetics model (see [40]) with a different functional form for the chemotactic sensitivity function. Namely, we shall take into account the prevention of overcrowding effect, sometimes also referred to as 'volume-filling' effect, assuming a density-dependent sensitivity function comprising saturation, where ψ is the maximal chemotactic rate.

2.2 Chemoattractants: proinflammatory cytokines $\tilde{c}(T, \mathbf{X})$

The evolution of the density of cytokines is ruled by the following equation:

$$\frac{\partial \tilde{c}}{\partial T} = \frac{1}{\nu}\left(\underbrace{\varepsilon \Delta_{\mathbf{X}} \tilde{c}}_{\text{Diffusion}} + \underbrace{\mu \tilde{d} + b\tilde{m}}_{\text{Production}} - \underbrace{\alpha \tilde{c}}_{\text{Decay}} \right). \tag{2}$$

The first term on the right hand side of Eq.(2) describes undirected random diffusion of the cytokines with diffusivity coefficient ε. We assume that the chemotactic signal, consisting of the cytokine, is produced by both the the damaged oligodendrocytes and activated macrophages. The production of the chemical signal by the olygodendrocytes, also proposed in [15], is a modeling assumption which expresses the onset of protective mechanisms from damaged cells in which, by local recruiting the surrounding macrophages, they protect the neighboring zones from insults. The activation of protecting processes in the early stages of active lesions has been recently reported in [66] and, other than being responsible for the formation of the concentric patterns typical of Balò sclerosis, could account for the relatively slow progress of pre-demyelinated lesions before the appearance of the classical inflammatory demyelinated plaque which is observed in MRI [95]. In the present model we also introduce a production term of proinflammatory cytokines by activated macrophages. In fact, it is well known that microglial cells are able to release a wide range of soluble mediators, ranging from cytotoxic mediators to trophic factors, which can exert deleterious as well as neuroprotective effects on the surrounding tissue. Several studies have resulted in the definition of different activation states: M1 'classically activated' microglia are considered to be neurotoxic and damaging to oligodendrocytes, whereas the alternative M2 phenotype promotes repair. Since we are interested in describing the initial stage of formation of the plaques, we will not take into account the production from microglia of repair-promoting effector and precursor cells, which usually play a key role in preactive and remyelinating lesions, and only consider the release of proinflammatory cytokines by activated macrophages as they are involved in the up-regulation of the inflammatory reaction.

Therefore the chemical kinetics consist of cell-dependent chemical production and linear degradation. To keep the kinetic term simple, we consider cell proliferation and death independent of the chemical signal and assume μ, b and α to be constant proliferation and death coefficients, respectively. Finally, as we want also to model the possibility for the chemoattractant cytokine dynamics to evolve on a different time scale compared to the other species, we consider its characteristic time scale ν as a parameter.

2.3 Destroyed oligodendrocytes $\tilde{d}(T, \mathbf{X})$

Finally, the evolution of the density of damaged oligodendrocytes is ruled by the following equation:

$$\frac{\partial \tilde{d}}{\partial T} = \underbrace{\kappa F(\tilde{m})\tilde{m}\left(\bar{d}-\tilde{d}\right)}_{\text{Production}}, \qquad \text{with} \quad F(\tilde{m}) = \frac{\tilde{m}}{\bar{m}+\tilde{m}} \tag{3}$$

We assume that the destroyed oligodendrocytes are immotile, so that we do not consider any spatial dynamics for them. Moreover, denoting by $\bar{d}$ the initial characteristic density of oligodendrocytes in the brain, intact oligodendrocytes are destroyed upon interaction with activated macrophages with a mass action law, the parameter κ measuring the destructive strenght of the macrophages. The damaging function F has been chosen to be positive and increasing with saturation for high values of the macrophages density, and is borrowed from [15, 48].

2.4 Non-dimensional form of the equations

Putting together Eqs.(1)-(3), the interaction between the three species can be described by the following system of PDEs:

$$\begin{cases} \frac{\partial \tilde{m}}{\partial T} = D\Delta_{\mathbf{X}}\tilde{m} + \lambda\tilde{m}(\bar{m}-\tilde{m}) - \nabla_{\mathbf{X}}\cdot(\Psi(\tilde{m})\nabla_{\mathbf{X}}\tilde{c}), & \text{with} \quad \Psi(\tilde{m}) = \psi\frac{\tilde{m}}{\bar{m}+\tilde{m}}, \\ \frac{\partial \tilde{c}}{\partial T} = \frac{1}{\nu}\left[\varepsilon\Delta_{\mathbf{X}}\tilde{c} + \mu\tilde{d} - \alpha\tilde{c} + b\tilde{m}\right], & \\ \frac{\partial \tilde{d}}{\partial T} = \kappa F(\tilde{m})\tilde{m}\left(\bar{d}-\tilde{d}\right), & \text{with} \quad F(\tilde{m}) = \frac{\tilde{m}}{\bar{m}+\tilde{m}}, \end{cases} \tag{4}$$

Setting the reduced variables and parameters as

$$\begin{aligned} &m = \frac{\tilde{m}}{\bar{m}} \quad d = \frac{\tilde{d}}{\bar{d}} \quad c = \frac{\alpha}{\bar{b}\bar{m}}\tilde{c} \quad t = \lambda\bar{m}T \quad x = \sqrt{\frac{\lambda\bar{m}}{D}}X \\ &\chi = \frac{\psi\bar{b}}{\alpha D} \quad \tau = \frac{\nu\lambda\bar{m}}{\alpha} \quad \epsilon = \frac{\varepsilon\lambda\bar{m}}{\alpha D} \quad \beta = \frac{b}{\bar{b}} \quad r = \frac{\kappa}{\lambda} \quad \delta = \frac{\mu\bar{d}}{\bar{m}\bar{b}}, \end{aligned} \tag{5}$$

where $\bar{b}$ is a typical production rate per macrophage and $\bar{d}$ is the characteristic density of intact oligodendrocytes in the brain, it follows that the non-dimensional form of Eqs.(1)-(3) yields the following PDE system:

$$\begin{cases} \frac{\partial m}{\partial t} = \Delta m + m(1-m) - \nabla\cdot(\chi(m)\nabla c), & \text{with} \quad \chi(m) = \chi\frac{m}{1+m}, \\ \frac{\partial c}{\partial t} = \frac{1}{\tau}\left[\epsilon\Delta c + (\delta d - c + \beta m)\right] & \\ \frac{\partial d}{\partial t} = rF(m)m(1-d) & \text{where } F(m) = \frac{m}{1+m} \end{cases} \tag{6}$$

which we shall solve in $(t,x) \in \mathbb{R}^+ \times \Omega$, $\Omega \subset \mathbb{R}^n$, $n = 1, 2$ imposing no-flux boundary conditions and in the following ranges of the parameters:

$$\chi > 0, \qquad \tau > 0, \qquad \epsilon > 0, \qquad \beta \geq 0, \qquad r > 0, \qquad \delta \geq 0. \tag{7}$$

The mathematical properties of the Keller-Segel system and its numerous variations have been extensively studied in recent years [25, 39, 46, 47, 93]. In particular, a property that has deserved a lot of attention is the fact that solutions might blow-up in finite time. Well-posedness of the model relies on the choice of the sensitivity function and on the inclusion of growth and degradation terms. If the sensitivity function depends linearly or logarithmically on m and in absence of growth or decay terms, global existence has been proved in one spatial dimension [21]. In two dimensions global existence has been proved only if the initial mass of the cell density is below a given threshold [14].

In the case when volume filling effects are considered, global existence and uniqueness of the Cauchy problem with both linear and nonlinear diffusion has been proved by Burger et al. [13]. Moreover the inclusion

of logistic-type growth restrictions has been detected to prevent blow-up of the solutions. In particular in presence of growth and degradation terms, global well posedness has been recently proved for a model of residential burglaries where a logarithmic sensitivity function was considered [83, 84]. The global boundedness and finite-time blow-up of solutions for a chemotaxis system with generalized volume-filling effect and logistic source has been studied in [96, 97].

A large body of literature is also devoted to the existence of non-constant steady states for Keller-Segel type models, which shows that the interplay of the chemotactic term and cell kinetics of logistic form may lead to pattern formation and, more generally, to a very rich dynamics ([50, 64, 90, 94] just to mention some recent contributions). In particular, in [63] it has been analytically proved that the volume-filling chemotaxis model with logistic source term can develop, other than stationary patterns, a variety of interesting spatio-temporal patterns, such as chaotic dynamics and merging processes.

Our interest is mainly devoted to the process leading to the formation of plaques of destroyed oligodendrocytes, therefore in what follows we shall investigate the conditions under which spatial patterns can arise for the system (6).

3 Turing instability analysis

In this section we shall perform a linear stability analysis of system (6) to investigate the formation of stationary structures around the homogeneous steady state $(m^*, c^*, d^*) = (1, \beta+\delta, 1)$. This is intended to explore the long-time dynamics of the system (6) and, from a biological point of view, to give a quantitative description of the clusters of cells observed when the majority of the present macrophages are turned into the active state and most of the oligodendrocytes are destroyed.

The two uniform steady states of the system are the disease-free equilibrium $P_0 = (0,0,0)$ and the non trivial point $P^* = (m^*, c^*, d^*) = (1, \beta+\delta, 1)$. The equilibrium P_0 is unstable while P^* is a stable attractive node for the kinetics for all non negative values of the parameters.

Linearization around this latter steady state, gives the system:

$$\dot{\mathbf{w}} = J'\mathbf{w} + D'\Delta\mathbf{w}, \qquad \text{where } \mathbf{w} = \begin{pmatrix} m-m^* \\ c-c^* \\ d-d^* \end{pmatrix}, \tag{8}$$

$$J' = \begin{pmatrix} -1 & 0 & 0 \\ \frac{\beta}{\tau} & -\frac{1}{\tau} & \frac{\delta}{\tau} \\ 0 & 0 & -\frac{r}{2} \end{pmatrix}, \qquad \text{and} \qquad D' = \begin{pmatrix} 1 & -\frac{\chi}{2} & 0 \\ 0 & \frac{\epsilon}{\tau} & 0 \\ 0 & 0 & 0 \end{pmatrix}. \tag{9}$$

We look for solutions of the form $\mathbf{w} \propto e^{\sigma t + i\mathbf{k}\cdot\mathbf{x}}$, where σ represents the linear growth rate and $\mathbf{k}$ is the wavenumber of the perturbation. Upon substitution into (8), one easily gets that one of the eigenvalues is equal to $-r/2$. Therefore we are left with the following dispersion relation, which gives the eigenvalue σ as a function of the wavenumber $k = |\mathbf{k}|$:

$$\sigma^2 + g(k^2)\sigma + h(k^2) = 0, \tag{10}$$

with

$$h(k^2) = det(D)k^4 + qk^2 + det(J), \tag{11}$$

and

$$g(k^2) = k^2 tr(D) - tr(J), \qquad q = \frac{2(1+\epsilon) - \chi\beta}{2\tau},$$

where

$$J = \begin{pmatrix} -1 & 0 \\ \frac{\beta}{\tau} & -\frac{1}{\tau} \end{pmatrix}, \qquad \text{and} \qquad D = \begin{pmatrix} 1 & -\frac{\chi}{2} \\ 0 & \frac{\epsilon}{\tau} \end{pmatrix}.$$

For the Turing instability to occur, the steady state has to be linearly unstable to spatial disturbances, i.e. we require that $\exists\, k \neq 0 :\ \mathrm{Re}\{\sigma(k^2)\} > 0$. By inspection it is easiliy seen that $g(k^2) > 0\ \forall k$. Therefore the only possibility for (10) to have a root $\sigma(k^2) > 0$ is $h(k^2) < 0$ for some nonzero k (see e.g. [71] pages 84-85). We denote by k_c the value where $h(k^2)$ attains its minimum. Obviously k_c depends on the bifurcation parameter χ. Marginal stability is where $h(k_c^2) = 0$. Therefore the bifurcation value χ_c and the most unstable mode k_c can be found imposing:

$$\min_k(h(k^2)) = 0. \tag{12}$$

The minimum of h is attained when

$$k^2 = -\frac{q}{2det(D)} \equiv k_c^2. \tag{13}$$

The previous expression for the critical wavenumber requires $q < 0$, which is satisfied by imposing the additional necessary condition:

$$\chi > \bar{\chi} = \frac{2(\epsilon+1)}{\beta}.$$

Figure 1 shows the graph of $h(k^2)$ and its dependence on the chemotaxis parameter χ, which plays the role of the bifurcation parameter. Inserting the expression (13) for k_c^2 in (11), and imposing (12) one can find the bifurcation value:

$$\chi_c = \frac{2(\sqrt{\epsilon}+1)^2}{\beta}. \tag{14}$$

The corresponding critical wavenumber can be found inserting the above expression in (13):

$$k_c^2 = \frac{1}{\sqrt{\epsilon}}. \tag{15}$$

Since $\bar{\chi} < \chi_c$, for $\chi > \chi_c$ the system admits a range $[{k_1}^2, {k_2}^2]$ of unstable wavenumbers. Thus, to allow for the possibility of pattern formation, the linear dimension of the domain must be big enough so that at least one of the modes admitted by the boundary conditions falls within the interval $[{k_1}^2, {k_2}^2]$. We have therefore proved the following

Theorem 1 (Turing instability) *Under the hypotheses* (7) *on the parameters, the equilibrium* (m^*, c^*, d^*) *is stable for the kinetics of model* (6)*. Moreover, if* $\chi > \chi_c$*, with* χ_c *given by* (14)*, then the uniform steady state solution* (m^*, c^*, d^*) *is an unstable equilibrium for the reaction-diffusion system* (6) *and a Turing bifurcation is possible.*

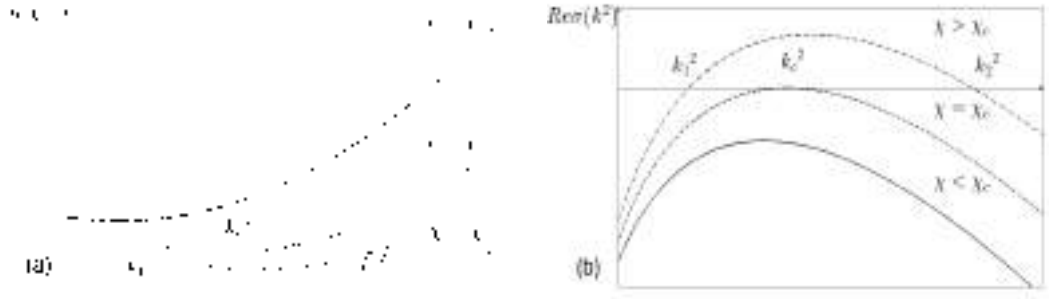

Fig. 1 (a) Plot of $h(k^2)$ as a function of the bifurcation parameter χ, showing the range of unstable wavenumbers for different values of χ. (b) Plot of the real part of the growth rate of the kth mode: a band of growing modes is present for $\chi > \chi_c$

4 Parameter Estimates

In order to estimate the relevant parameters introduced in the equations (1)-(3) and to be able to compare numerical predictions with experimental data, we take into account both preexisting literature and analogous quantities found in similar systems modeling inflammatory diseases, e.g. [48, 60]. From previous experimental estimates we can deduce the numerical values of all the involved parameters, but two: the activation rate of macrophages, λ, and the cytokine production rate per oligodendrocyte, μ/ν. We can estimate λ from imposing a typical linear size of the plaques. The order of magnitude of this numerical estimate has also been confirmed by another heuristic argument (see below). The parameter μ/ν has been introduced by Khonsari and Calvez in their model and we could not find any experimental data providing quantitative measures on the destroyed oligodendrocytes-driven cytokine production rates. Therefore, we shall assume a typical numerical value for μ/ν to be of the same order of magnitude of the macrophage-driven cytokine production rate and, to investigate

a whole range of possibilities, we allow μ/ν to vary in an interval ranging from zero to the typical value. However, since one of the aims of this study is to explore different scenarios that can emerge from the model, values were generally varied over wide ranges.

The set of parameter values available from experimental data with the corresponding units and descriptions is provided in Table 1.

We assume a default average density of inactive macrophages $\bar{m}$, as well as the distribution of healthy oligodendrocytes $\bar{d}$, evenly spread in the white matter of the brain based on the experiments reported in [73] and [61], respectively and also adopted by [48].

The motility of macrophages has been extensively studied experimentally in literature, therefore we use the rate of random motion of activate macrophages D as given by [69].

We could not find in literature any estimated value of ψ, the parameter that expresses the maximal rate for the chosen form of the chemotactic flux of activated macrophages $\psi \frac{\tilde{m}}{\tilde{m}+\bar{m}} \nabla_{\mathbf{X}} \tilde{c}$. Therefore, we derived an estimate of the numerical value of ψ using the experimentally measured data reported in [69] of the parameter $\bar{\chi}$, which is the chemotactic coefficient of the following flux of neutrophils: $\bar{\chi}\tilde{m}\nabla_{\mathbf{X}}\tilde{c}$. In fact one can easily observe that, for small values of the macrophages density ($\tilde{m} \ll \bar{m}$), $\psi \simeq \bar{\chi}\bar{m}$. Therefore, since $\bar{\chi} \in [6, 780]$ $\mu\text{m}^2 \cdot \text{nM}^{-1} \cdot \text{min}^{-1}$ and recalling that $\text{nM} = 10^{-9} \cdot \text{Mwt} \cdot \text{pg} \cdot \mu\text{m}^{-3}$, where Mwt is the molecular weight of the cytokine expressed in kDa (we used the value of 17 kDa for the molecular weight of IL-1β), we obtained for ψ the range of values given in Table 1.

The activation rate of macrophages λ has not been measured in experimental literature. Therefore, our estimate of this parameter is obtained by imposing that the typical length scale of the system $\sqrt{D/(\lambda\bar{m})}$ is 0.258 mm. This choice allows to describe plaques with size ranging from small to large, consistently with the reported linear dimensions of the active lesions which can vary between few millimeters to centimeter [56, 66]. With the above assumed values of D and $\bar{m}$, we obtain $\lambda \sim 3 \cdot 10^{-6}$ $\text{mm}^2 \cdot \text{cells}^{-1} \cdot \text{min}^{-1}$ and, consequently, a characteristic time scale ~ 0.7 days. This is consistent with the findings of some recent MRI studies according to which plaques in MS can start their genesis several hours or days before the appearance of the inflammatory demyelinating lesions [2, 18]. Indeed, the same order of magnitude for the value of λ can be obtained from an heuristic reasoning based on the explicit solution of the logistic equation, which rules the activation rate of the microglia. In fact, assuming that the initial datum is given by the density of the activated macrophages in a healthy individual, namely ~ 100 cells mm^{-2} [60], and that the density of activated macrophages at three times the characteristic time attains the 90% of its asymptotic value, one gets $\lambda \simeq 3.43 \cdot 10^{-6}$ $\text{mm}^2 \cdot \text{cells}^{-1} \cdot \text{min}^{-1}$, in good agreement with the above chosen value of λ.

The diffusivity coefficient of cytokines ε has been evaluated by the known direct determination of the diffusion constant for a given molecule in the aqueous cytoplasm of mammalian cells (namely $\sim 3.3 \cdot 10^{-6}\text{cm}^2\text{sec}^{-1}$ for a molecular weigth of 0.17 kDa) and by considering that it scales with the cube root of the molecular weight of the species involved, (this procedure was also adopted in [60]).

To calculate the numerical value of the typical production rate of cytokine per macrophage ($\bar{b}/\nu$), we use data from in vitro experiments [59, 72]. Since the production rate of cytokine per macrophage ranges in the interval $5.7 \cdot 10^{-6} - 1.96 \cdot 10^{-5}$ $\text{pg} \cdot \text{min}^{-1} \cdot \text{cells}^{-1}$, we choose $\bar{b}/\nu = 1.96 \cdot 10^{-5}$ $\text{pg} \cdot \text{min}^{-1} \cdot \text{cells}^{-1}$, so that the adimensional parameter $\beta = (b/\nu)/(\bar{b}/\nu)$ ranges in the interval $[0.3, 1]$.

The cytokine production rate μ per oligodendrocyte is not derived in literature, therefore we estimate its value assuming that the two different contributions to the cytokine production coming from the activate macrophages and the damaged oligodendrocytes are of comparable size. Therefore, we choose μ/ν to vary in the range $10^{-6} - 10^{-5}$ pg min^{-1} cells^{-1}. The numerical values of cytokine decay rate α are taken from [72].

A numerical estimate of the damaging intensity by macrophages on oligodendrocytes κ is provided in [48]. Here, taking into account the fact that the demyelination process in MS is less aggressive than in Baló's form of sclerosis, we shall consider a wider range of variation of κ, which will allow us to explore several scenarios corresponding to varying levels of aggressiveness of the disease.

The range of admissible dimensionless parameter values arising from the above scaling and used in the numerical simulations is listed in Table 2.

5 Pattern formation in 1D domain

To provide insights on the possible dynamics supported by the model system we have first explored the pattern-forming properties of system (6) on $1D$ spatial domains. Depending on the values of the system parameters, we have detected two different scenarios of transition from the homogeneous to the patterned state: a supercritical transition and a subcritical transition. When the bifurcation occurs supercritically, at the bifurcation value χ_c the homogeneous equilibrium becomes linearly unstable and a stable pattern branch is originated whose amplitude scales as the square root of the distance to the transition point. In the case of subcritical bifurcation,

Table 1 Dimension carrying parameter values of the model

Parameter	Description	Value	Source
$\bar{m}$	average macrophages density	350 cells mm^{-2}	[73]
$\bar{d}$	average oligodendrocyte density	400 cells mm^{-2}	[61]
λ	macrophages activation rate	$\sim 3 \cdot 10^{-6}$ mm^2 cells^{-1} min^{-1}	Estimated
D	macrophages random motility	$6.6 \cdot 10^{-5}$ mm^2 min^{-1}	[69]
ψ	chemoattraction	$0.0023 - 0.298$ mm^2 min^{-1} cells pg^{-1}	Derived from [69]
ε/ν	cytokine diffusion	$9 \cdot 10^{-4}$ mm^2 min^{-1}	[35]
b/ν	cytokine production rate	$5.7 \cdot 10^{-6} - 1.96 \cdot 10^{-5}$ pg min^{-1} cells^{-1}	[59, 72]
μ/ν	cytokine production rate per oligodendrocyte	$10^{-6} - 10^{-5}$ pg min^{-1} cells^{-1}	Estimated
α/ν	cytokine decay rate	$0.001 - 0.03$ min^{-1}	[72]
κ	damaging intensity	$3.96 \cdot 10^{-6}$ mm^2 cells^{-1} min^{-1}	[48]

Table 2 Non dimensional parameter values used in the numerical simulations

Parameter	Description	Value
χ	chemoattraction	$4 - 55$
τ	time scale of cytokine dynamics	$0.001 - 1$
ϵ	cytokine diffusion	$0.5 - 1.5$
β	cytokine production rate	$0.2 - 1$
δ	cytokine production rate per oligodendrocyte	$0 - 1$
r	damaging intensity	$0.01 - 6$

the system becomes linearly unstable above the bifurcation threshold but a finite amplitude pattern branch exists also below this value. Moreover, the amplitude of the resulting pattern does not converge to zero as the bifurcation threshold is approached from above. Therefore, in the subcritical case and below the transition point, the homogeneous equilibrium is bistable with the Turing pattern: a sufficiently large perturbation can in fact drive the system toward the nontrivial stable stationary state and hysteretic behavior is possible. The detection of a subcritical transition is both of theoretical and biological interest since it provides the possibility of stable localized stationary patterns [44]. However the supercritical vs subcritical character of the bifurcation cannot be discerned by the linear stability analysis outcomes and it is necessary to perform a weakly nonlinear expansion to derive the corresponding amplitude equations which yield the form of the pattern close to criticality. This is performed in Subsection 5.1. In Subsection 5.2 a numerical bifurcation analysis far from transition is then set forward which shows the appearance of complex spatio-temporal phenomena.

5.1 Weakly nonlinear analysis

In this section we shall derive the amplitude equations for the spatially periodic solutions to the system (6): through the multiple scales method we shall perform a weakly non linear analysis close to the uniform steady state $P^* = (m^*, c^*, d^*) = (1, \beta + \delta, 1)$. We shall adopt the formalism of [87] in which the authors extended the analysis presented in [67] where only two time scales had been considered; see also [22] considering the case of a $2D$ domain and the more recent papers [11, 31, 33, 34]. The intersted reader is referred to [92] where different approaches to WNL are compared.

We set a small control parameter $\eta^2 = (\chi - \chi_c)/\chi_c$, which gives the dimensionless distance of χ from the bifurcation value χ_c. Upon translation of the equilibrium P^* to the origin, the system (6) can be written as:

$$\frac{\partial \mathbf{w}}{\partial t} = \mathcal{L}^{\chi}\mathbf{w} + \mathcal{N}\mathbf{w}, \tag{16}$$

where $\mathbf{w}$ is defined in (8), the linear operator $\mathcal{L}^{\chi} = J' + D'(\chi)\partial_{xx}$ with J' and D' defined in (9), and $\mathcal{N}$ is a nonlinear operator containing higher order powers in $\mathbf{w}$.

Close to equilibrium we expand $\mathbf{w}$ and the bifurcation parameter χ as follows:

$$\begin{aligned} \mathbf{w} &= \eta\mathbf{w}_1 + \eta^2\mathbf{w}_2 + \eta^3\mathbf{w}_3 + O(\eta^4), \\ \chi &= \chi_c + \eta^2\chi_2 + O(\eta^4), \end{aligned}$$

and look for solutions having a multiple scale dependence on time t

$$\mathbf{w}_i = \mathbf{w}_i(T_2, T_4, \ldots)$$

where

$$T_2 = \eta^2 t, \quad T_4 = \eta^4 t, \ldots.$$

so that the time derivative operator has the following expansion:

$$\frac{\partial}{\partial t} = \eta^2 \frac{\partial}{\partial T_2} + \eta^4 \frac{\partial}{\partial T_4} + O(\eta^5).$$

We introduce the following notation: $\mathbf{w}_i = (w_{m_i}, w_{c_i}, w_{d_i})^T$ and:

$$\xi(m) = \frac{m}{1+m}, \qquad \phi(m,d) = \frac{m^2}{1+m}(1-d).$$

By substitution of the above expansions into (16) and collecting the terms at each order in η, we obtain the following systems:

$$O(\eta): \qquad \mathcal{L}^{\chi_c}\mathbf{w}_1 = \mathbf{0}, \tag{17}$$

$$O(\eta^2): \qquad \mathcal{L}^{\chi_c}\mathbf{w}_2 = \mathbf{F}, \tag{18}$$

$$O(\eta^3): \qquad \mathcal{L}^{\chi_c}\mathbf{w}_3 = \mathbf{G}, \tag{19}$$

with $\mathcal{L}^{\chi_c} = J' + D'(\chi_c)\partial_{xx}$ and the expressions for $\mathbf{F}$ and $\mathbf{G}$ are the following:

$$\mathbf{F} = \begin{pmatrix} w_{m_1}^2 \\ 0 \\ r\partial_{md}\phi(m^*,d^*) w_{m_1} w_{d_1} \end{pmatrix} + \chi_c \begin{pmatrix} \xi'(m^*)\partial_x \left(w_{m_1} \partial_x w_{c_1} \right) \\ 0 \\ 0 \end{pmatrix} \tag{20}$$

$$\begin{aligned} \mathbf{G} = & \begin{pmatrix} 2w_{m_1} w_{m_2} \\ 0 \\ r\left[\partial_{md}\phi(m^*,d^*) \left(w_{m_1} w_{d_2} + w_{m_2} w_{d_1} \right) + \frac{1}{2}\partial_{mmd}\phi(m^*,d^*) w_{m_1}^2 w_{d_1} \right] \end{pmatrix} \\ & + \chi_c \begin{pmatrix} \xi'(m^*)\partial_x \left(w_{m_1}\partial_x w_{c_2} + w_{m_2}\partial_x w_{c_1} \right) + \frac{\xi''(m^*)}{2}\partial_x \left(w_{m_1}^2 \partial_x w_{c_1} \right) \\ 0 \\ 0 \end{pmatrix} \\ & + R(\chi_2)\partial_{xx}\mathbf{w}_1, \end{aligned} \tag{21}$$

where

$$R(\chi_2) = \begin{pmatrix} 0 & \chi_2 \xi(m^*) & 0 \\ 0 & 0 & 0 \\ 0 & 0 & 0 \end{pmatrix}. \tag{22}$$

From equation (17), by imposing Neumann boundary conditions, one gets a solution of the form:

$$\mathbf{w}_1 = \rho A(T_2, \ldots)\cos(k_c x), \quad \text{where } \rho \in Ker(J' - k_c^2 D'(\chi_c)), \tag{23}$$

where $A(T_2, \ldots)$ is the amplitude of the pattern. Notice that k_c has to be compatible with the Neumann boundary condition; in a 1D domain $[0, L]$, for example, it is required that $k_c = n\pi/L$ for some $n \in \mathbb{N}$. In practice, when comparing the results of an accurate numerical resolution of the system, with the predictions of the WNL analysis, one should tune the domain size to fit the above compatibility condition.

The solvability condition for the Eq. (18) is given by $\langle \mathbf{F}, \boldsymbol{\psi}\cos(k_c x)\rangle = 0$, with $\boldsymbol{\psi} \in Ker(\mathcal{L}^*)$, where we have denoted by $\mathcal{L}^*$ the adjoint of $\mathcal{L}^{\chi_c}$ and by $\langle \cdot, \cdot \rangle$ the scalar product in $L^2(0, 2\pi/k_c)$. The solvability condition is automatically satisfied and the solution $\mathbf{w}_2$ to the second-order system (18) can be easily written. Substituting $\mathbf{w}_1$ and $\mathbf{w}_2$ into (19), one gets the following expression for $\mathbf{G}$:

$$\mathbf{G} = \left(\frac{\partial A}{\partial T_2}\rho + A\mathbf{G}_1^{(1)} + A^3 \mathbf{G}_1^{(3)} \right) cos(k_c x) + \mathbf{G}^*. \tag{24}$$

In the above expression $\mathbf{G}^*$ satisfies the Fredholm solvability condition, while $\mathbf{G}_1^{(j)}$ for $j = 1, 3$, whose explicit expression is not reported here, depend on the system parameters. Therefore, imposing the solvability condition at the third order, we get the following Stuart-Landau equation for the amplitude $A(T_2)$:

$$\frac{\partial A}{\partial T_2} = \sigma A - L A^3, \tag{25}$$

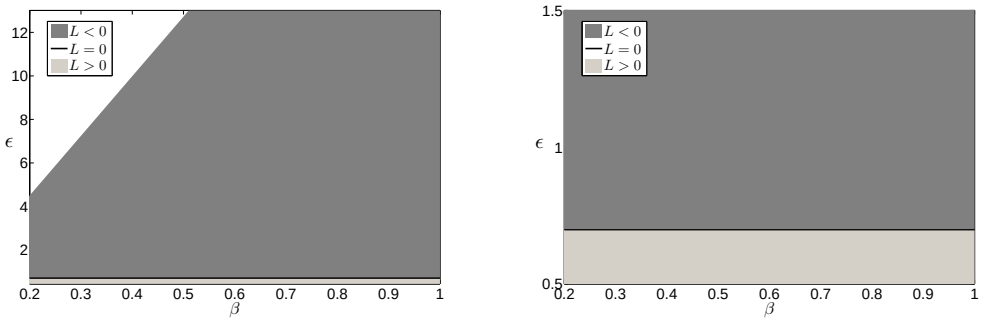

Fig. 2 (a) Turing region: The black bold line corresponds to $L(\epsilon,\beta)=0$. The region in light grey corresponds to the supercritical case $L>0$, whereas the dark grey region corresponds to the subcritical case $L<0$. The parameters are fixed as follows: $\tau=1,\delta=1,r=1,\chi=55$. (b) Magnification of (a) in the region of the parameters used in our simulations: $\epsilon=0.5-1.5$, $\beta=0.2-1$.

where:

$$\sigma=\frac{\langle \mathbf{G}_1^{(1)},\boldsymbol{\psi}\rangle}{\langle \boldsymbol{\rho},\boldsymbol{\psi}\rangle},\qquad L=\frac{\langle \mathbf{G}_1^{(3)},\boldsymbol{\psi}\rangle}{\langle \boldsymbol{\rho},\boldsymbol{\psi}\rangle}. \tag{26}$$

All the details of the derivation of the coefficients in Eq. (25) can be found in [4], where we have performed the weakly non linear analysis to investigate the pattern invasion as a travelling wave front.

One can easily see that the growth rate σ is always positive in all the pattern-forming region. Then the dynamics of the Stuart-Landau equation (25) can be divided into two qualitatively different cases depending upon the sign of the Landau coefficient L: the supercritical case, that corresponds to $L>0$, and the subcritical case, corresponding to $L<0$. From the analytical expression of the Landau coefficient, we can deduce that it only depends on the parameters β and ϵ. In Figs. 2(a)-(b) we present the curve across which $L(\epsilon,\beta)$ changes its sign for the following set of parameters: $\tau=1,\delta=1,r=1,\chi=55$. This curve corresponds to a straight line of equation $\epsilon\approx 0.697$. It divides the Turing space into two distinct regions: the region where the pattern forms supercritically (displayed in light grey) and the subcritical region (displayed in dark grey).

In the supercritical case, the Stuart Landau equation (25) has a stable equilibrium solution $A_\infty=\sqrt{\sigma/L}$, that is the asymptotic value of the amplitude $A(T)$ of the pattern.

Otherwise, in the subcritical case, i.e. when the Landau coefficient L is negative, the third order Stuart-Landau equation (25) is not able to capture the amplitude of the pattern. In this case we shall push the weakly non linear analysis to a higher order, thus by performing the weakly non linear analysis up to $O(\eta^5)$. This leads to the quintic Stuart-Landau equation for the amplitude of the pattern A:

$$\frac{\partial A}{\partial T_2}=\tilde{\sigma}A-\tilde{L}A^3+\tilde{Q}A^5, \tag{27}$$

where the explicit expression of the coefficients $\tilde{L},\tilde{\sigma}$ and $\tilde{Q}$ in (27) is too cumbersome and for brevity will be not reported here. We remark that in this case $\tilde{Q}$ is $O(\eta^2)$; this shows that the stationary solutions of (27) are $O(1/\eta)$ so that the amplitude of the pattern originated from the subcritical transition is $O(1)$.

5.2 Bifurcation analysis far from equilibrium

The numerical investigations of system (6) are addressed on the $1D$ spatial domain $[0,12\pi]$, which corresponds to about 1cm in the physical domain, imposing zero flux boundary conditions. The numerical scheme adopted is based on a method of lines that considers the discretization of the spatial operators and the time integration separately. The equations are first discretized in space with a finite-difference scheme on a 200 point grid for a domain of length 12π, and the resulting semi-discrete system of ODEs is then integrated in time.

The diffusion terms are approximated by second-order central differences and the taxis terms is approximated by a finite difference scheme that conserves the number of macrophages. All the $1D$ simulations were performed using the CVODE stiff integrator included in the XPPAUT computational software package. We set error tolerances of 10^{-10} in CVODE and used a time-step $\Delta t=10^{-3}$. We verified the dynamical behavior

of the solutions to (6), varying the mesh spacing Δx and the time step Δt, using the $1D$-version of spectral method adopted for the $2D$ simulations.

We have verified the outcomes predicted by the linear stability analysis and reported in Section 3, assigning as initial condition a small random perturbation of the stable homogeneous equilibrium. Namely, if the parameter bifurcation χ is chosen below the critical threshold, after some transient the system reaches the uniform equilibrium. A different picture depicts if one chooses the bifurcation parameter slightly above the Turing bifurcation value χ_c: the small random perturbation evolves towards a stationary non-homogeneous pattern for the species m and c, while, after a transient whose timescale is ruled by the parameter r during which nonhomogeneous structures emerge, no pattern persists in the asymptotic dynamics of the species d, which evolves towards the homogeneous equilibrium value $d = 1$, where all the present oligodendrocytes are destroyed.

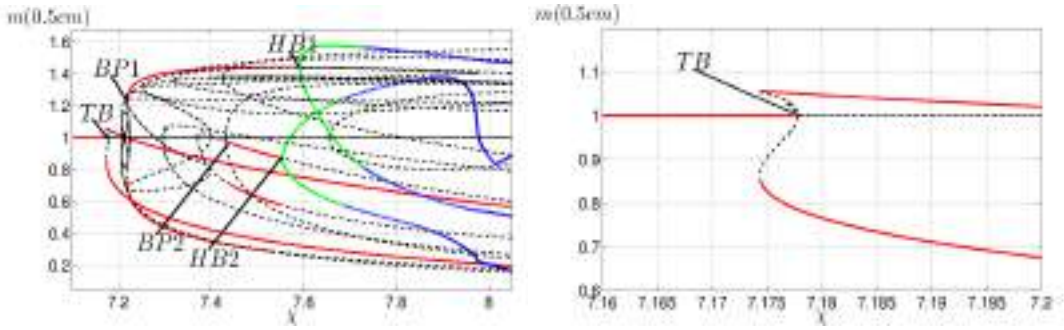

(a) (b)

Fig. 3 (a)The bifurcation diagram as the parameter χ is varied. Other parameters are fixed: $\epsilon = 0.8, \beta = 1, \delta = 1, r = 1, \tau = 1$. Stable and unstable stationary branches are depicted as red solid lines and black dashed lines respectively, stable and unstable oscillatory branches are depicted in green and blue, respectively. (b) Enlargement of the subcritical primary Turing Bifurcation close to χ_c

To gain some insight on far from equilibrium solutions, we have therefore numerically explored the system dynamics for different sets of the parameters and computed the corresponding bifurcation diagrams as the control parameter χ is varied. For parameter sets for which the primary Turing bifurcation occurred subcritically, secondary bifurcations and transition to irregular spatio-temporal solutions were often observed, as illustrated below.

In Fig.3(a) we show the bifurcation diagram computed using the numerical continuation software AUTO for $r = 1, \tau = 1, \epsilon = .8, \beta = 1, \delta = 1$ which yields $\chi_c \simeq 7.17$ and $k_c = 1.05$. The equilibrium amplitude of the central point $m(0.5cm)$ of the species m is shown for $\chi \in [7.1, 8.05]$. The corresponding bifurcation diagram for the species d returns the uniform stable equilibrium $d = 1$ for the whole interval of χ.

At the point labeled by TB, for $\chi \simeq 7.1775$, the uniform steady state first destabilizes through a subcritical Turing bifurcation. The area close to χ_c is magnified in Fig.3(b), which clearly shows the subcritical character of the bifurcation: for $7.174 \lesssim \chi \lesssim 7.1775$ the homogeneous equilibrium is bistable with the primary Turing pattern branch. Since $k_c \simeq 1.05$ on a domain size $L = 12\pi$ (in non-dimensional variables), one expects, on the basis of the linear analysis, $\simeq 6.5$ stripes in the simulations. The spatio-temporal evolution of the corresponding pattern on the primary Turing branch for $\chi \simeq 7.264$ is shown in Fig.4.

For $\chi = 7.22$, at the bifurcation point labeled by $BP1$ in Fig.3(a), a stable branch of stationary patterns emerge from an unstable branch. The existence of this branch of periodic solutions can be predicted by linear analysis: in fact as the distance of the parameter χ from the primary instability threshold is increased, more consecutive modes of the discrete spectrum allowed by the boundary conditions become unstable. The numerical simulation showing the form and amplitude of the pattern of m and c for $\chi \simeq 7.262$ is reported in Fig.5. It shows that the resulting pattern differs from the Turing pattern emerging from the primary bifurcation and obtained for the same value of the parameter χ, in both the amplitude and the wavenumber, as 6 stripes are now observed.

For $\chi \simeq 7.441$, at the bifurcation point labeled by $BP2$ in Fig.3(a), a stable branch of stationary patterns emerge from an unstable branch as a consequence of another mode driven unstable by the increased value of the bifurcation parameter. The numerical simulation which displays the form and amplitude of the pattern of m and c for $\chi \simeq 7.498$ is reported in Fig.6, showing the emergence of a periodic pattern with 5.5 stripes.

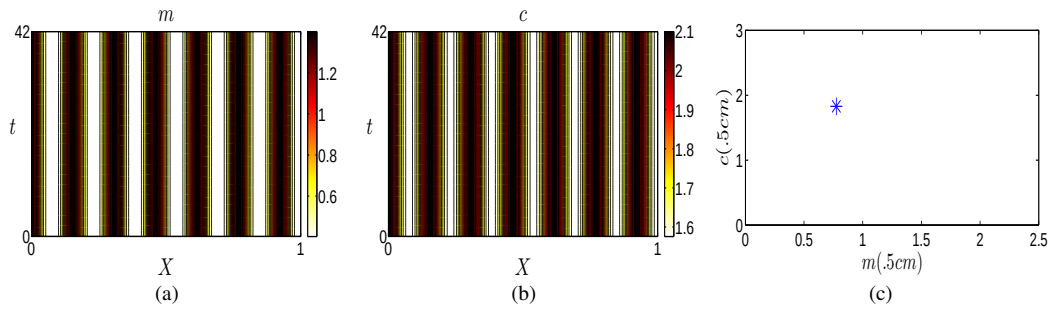

Fig. 4 (a)-(b): Spatio-temporal evolution of macrophages (a) and cytokines (b) in the case $\chi = 7.264 > \chi_c \simeq 7.1775$ on the stable stationary branch starting from the point labeled by TB in the bifurcation diagram (Fig.3). The cell density is plotted as a function of space (horizontal axis) and time (vertical axis). The parameters are chosen as in Fig.3. (c) (m, c) phase-plane at the midpoint location $X = 0.5cm$. The corresponding trajectory gives a fixed point, indicating the presence of a stationary pattern.

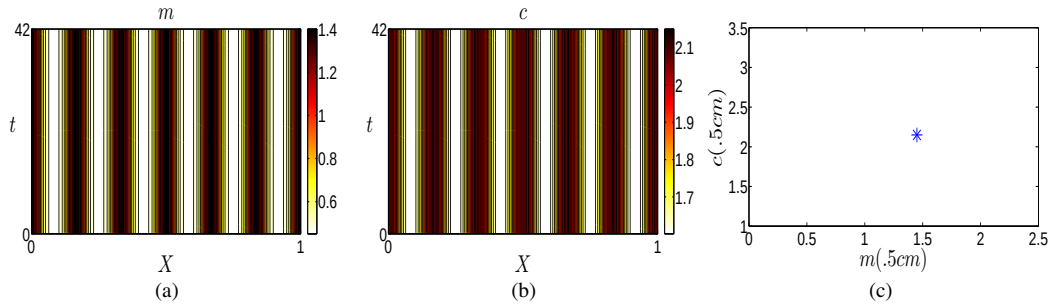

Fig. 5 (a)-(b): Spatio-temporal evolution of macrophages (a) and cytokines (b) in the case $\chi = 7.262 > \chi_c \simeq 7.1775$ on the stable stationary branch starting from the point labeled by $BP1$ in the bifurcation diagram (Fig.3(a)). The parameters are chosen as in Fig.3. This pattern has different amplitude and wavenumber from the pattern originated from the Turing bifurcation TB. (c) (m, c) phase-plane at the midpoint location $X = 0.5cm$. The corresponding trajectory gives a fixed point, indicating the presence of a stationary pattern.

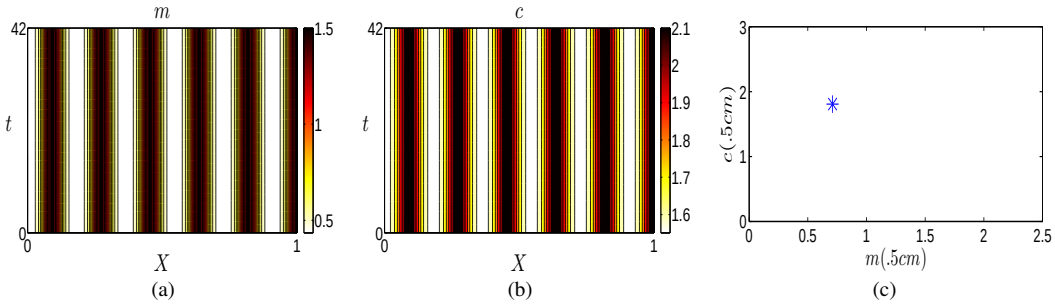

Fig. 6 (a)-(b): Spatio-temporal evolution of macrophages (a) and cytokines (b) in the case $\chi = 7.498 > \chi_c \simeq 7.1775$ on the stable stationary branch starting from the point labeled by $BP2$ in the bifurcation diagram (Fig.3(a)). The parameters are chosen as in Fig.3. This pattern differs in both amplitude and wavenumber from the pattern emerging from the Turing instability point. (c) (m, c) phase-plane at the midpoint location $X = 0.5cm$. The corresponding trajectory gives a fixed point, indicating the presence of a stationary pattern.

As χ is increased, this stationary branch remains stable up to the point labeled by $HB2$ for $\chi \simeq 7.554$, where a secondary supercritical Hopf bifurcation occurs. The simulation shown in Fig.7 presents the corresponding oscillatory solutions for $\chi \simeq 7.67$.

For $\chi \simeq 7.68$ the oscillatory branch loses stability and a torus bifurcation takes place at $\chi \simeq 7.69$. The corresponding space-time evolutions are shown in Fig.8.

We were unable to detect a period-doubling sequence to irregularity, which is commonly associated with chaotic dynamics, maybe for an insufficient resolution of the step increase in χ. Further increase in the chemotactic sensitivity parameter in fact results in more accentuated space-time irregularity, up to $\chi \simeq 8.1$,

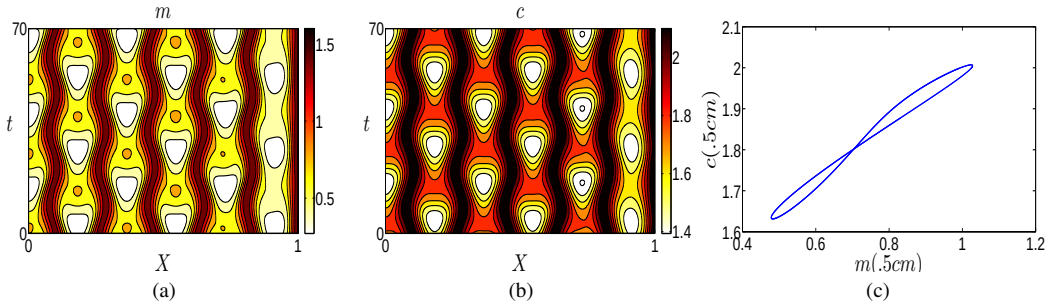

Fig. 7 (a)-(b): Spatio-temporal evolution of macrophages (a) and cytokines (b) in the case $\chi = 7.67 > \chi_c \simeq 7.1775$ on the stable oscillatory branch starting from the point labeled by $HB2$ in the bifurcation diagram (Fig.3 (a)). The parameters are chosen as in Fig.3. (c) (m, c) phase-plane at the midpoint location $X = 0.5cm$. The corresponding trajectory gives a closed trajectory, showing the presence of a Hopf bifurcation.

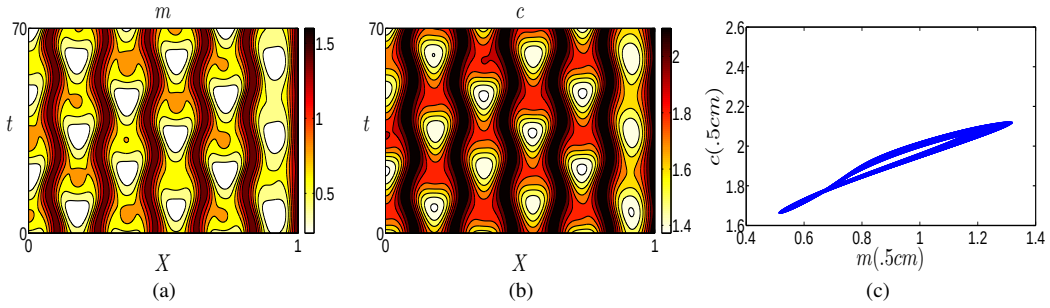

Fig. 8 (a)-(b): Spatio-temporal evolution of macrophages (a) and cytokines (b) in the case $\chi = 7.69 > \chi_c \simeq 7.1775$ on the unstable oscillatory branch starting from the point labeled by $HB2$ in the bifurcation diagram (Fig.3 (a)). The parameters are chosen as in Fig.3. (c) (m, c) phase-plane at the midpoint location $X = 0.5cm$. The corresponding trajectory shows the presence of a torus bifurcation.

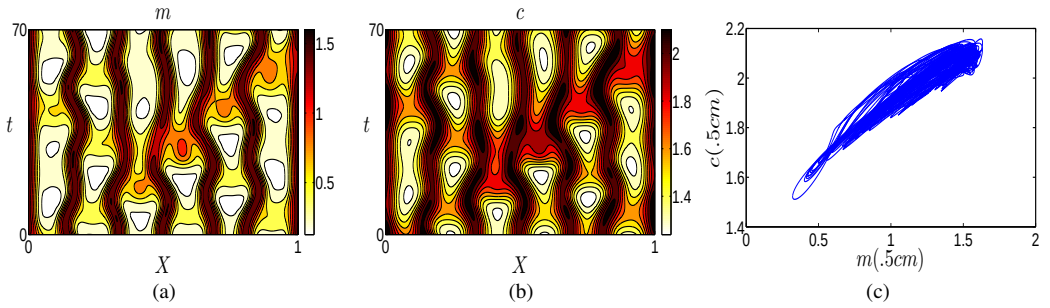

Fig. 9 (a)-(b): Spatio-temporal evolution of macrophages (a) and cytokines (b) in the case $\chi = 7.89 > \chi_c \simeq 7.1775$ on the unstable oscillatory branch starting from the point labeled by $HB2$ in the bifurcation diagram (Fig.3 (a)). The parameters are chosen as in Fig.3. (c) (m, c) phase-plane at the midpoint location $X = 0.5cm$. The corresponding trajectory displays highly irregular dynamics.

when it becomes impossible to follow the oscillations and the system settles on the stable stationary pattern. The irregular space-time evolution of the system for $\chi \simeq 7.89$ is showed in Fig.9.

At $\chi \simeq 7.59$ the stable Turing branch originated from the point $BP1$ looses stability through a supercritical Hopf bifurcation and a stable periodic oscillating pattern is created. The corresponding simulation for $\chi = 7.651$ is shown in Fig.10.

Analogously to what observed on the other branch, the supercritical Hopf branch loses stability as χ is further increased: at $\chi \simeq 7.727$ a torus bifurcation occurs whose corresponding pattern for $\chi \simeq 7.732$ is displayed in Fig.11.

As the value of χ is further increased along this branch, the (m, c) plane trajectories at the midpoint spatial location indicate the presence of closed orbits that tend to strange attractors, corresponding to highly irregular

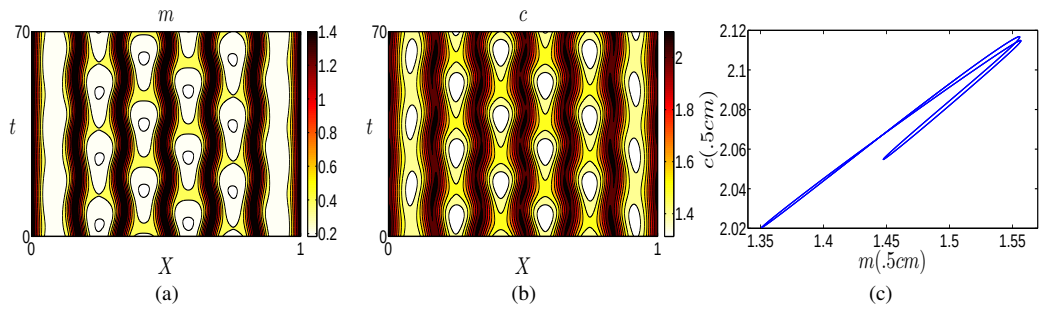

Fig. 10 (a)-(b): Spatio-temporal evolution of macrophages (a) and cytokines (b) in the case $\chi = 7.651 > \chi_c \simeq 7.1775$ on the stable oscillatory branch starting from the point labeled by $HB1$ in the bifurcation diagram (Fig.3). The parameters are chosen as in Fig.3. (c) (m, c) phase-plane at the midpoint location $X = 0.5cm$. The corresponding trajectory gives a closes trajectory.

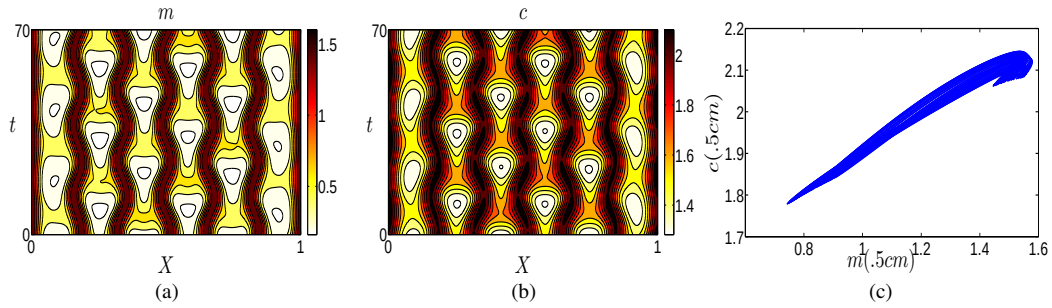

Fig. 11 (a)-(b): Spatio-temporal evolution of macrophages (a) and cytokines (b) in the case $\chi = 7.732 > \chi_c \simeq 7.1775$ on the stable oscillatory branch starting from the point labeled by $HB1$ in the bifurcation diagram (Fig.3). The parameters are chosen as in Fig.3. (c) (m, c) phase-plane at the midpoint location $X = 0.5cm$. The corresponding trajectory shows a torus bifurcation.

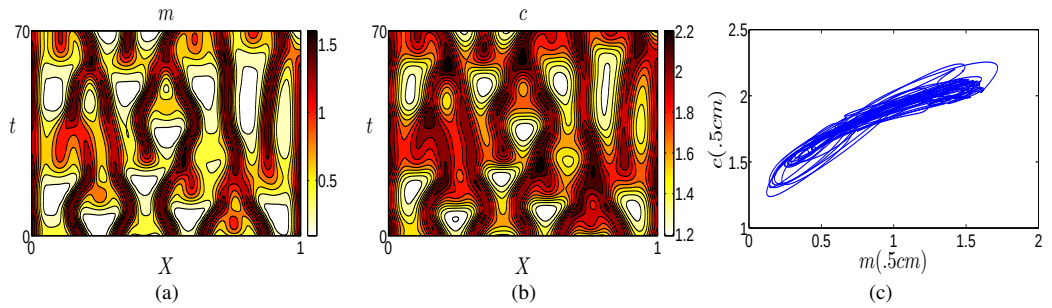

Fig. 12 Spatio-temporal evolution of macrophages (a) and cytokines (b) in the case $\chi = 8.06 > \chi_c \simeq 7.1775$ on the unstable oscillatory branch starting from the point labeled by $HB1$ in the bifurcation diagram (Fig.3 (a)). The parameters are chosen as in Fig.3. (c) (m, c) phase-plane at the midpoint location $X = 0.5cm$. The corresponding trajectory displays highly irregular dynamics.

space-time dynamics (see Fig. 12). As above, we failed to detect a possible period-doubling cascade, although this irregular behavior appeared robust with respect to variations in the parameter χ.

6 Numerical results in 2D domain

In this Section we present the results of the numerical investigations of the 2D spatio-temporal dynamics of the system (6). The aim here is to determine which parameters are likely to be most significant to affect the form and size of the plaques and to provide a quantitative analysis on the characterization of the demyelinated lesions. Different sets of parameters are used within the range listed in Table 2. In particular in the Subsection 6.1 we analyze four combinations of different aggressiveness levels, corresponding to different values of the parameter r, and of the cytokine production by macrophages, measured by the parameter β. The four combinations

are investigated in the Subsection 6.1.1 in absence of cytokine production by damaged oligodendrocytes ($\delta = 0$), and in the Subsection 6.1.2 for the moderate-high value of the cytokine production by damaged oligodendrocytes ($\delta = 1$). We prove that the phenomenon of formation of ringlike patterns is supported by the model system also in the absence of cytokine production from apoptotic oligodendrocytes: in fact in the case $\delta = 0$ stable patterns of concentric demyelination are observed when $\chi > \chi_c$. For each scenario we explore how the chemotactic parameter χ can influence the resulting emerging structures, performing the numerical simulations below and above the bifurcation threshold, and then discuss the influence of the parameters on the relevant features characterizing the lesions.

In Subsection 6.2 we fix a scenario with high aggressiveness (HA) and high cytokine production by the macrophages (HcP) and explore the effects produced by the variation of the cytokine diffusivity parameter ϵ. The last two Subsections are devoted to the study of the dynamics as the initial conditions are varied. In particular, in Subsection 6.3 we assign distinct initial spots for the macrophages species, showing the formation of a confluent plaque. In Subsection 6.4, we examine the effects produced by a random spatial initial perturbation for the concentration of activated macrophages. The following evolution closely resembles a pathological state known as pre-active lesions, reflecting the very early stages in the development of MS lesions.

We adopted a Fourier spectral solver on a square regular grid $Lx = Ly = 100$, which corresponds to a physical spatial domain of 2.58cm×2.58cm. The numerical algorithm is based on a two-stage second order semi-implicit time discretization scheme, i.e. a Runge-Kutta two Crank-Nicolson type, where the self diffusive term is treated implicitly and is of Crank-Nicolson type, and the non linear chemotactic term is evaluated explicitly. We used a computational grid with a resolution up to 2048×2048 points in a parallel computing environment. For all the simulations illustrated $\Delta t = 10^{-4}$.

In all the simulations presented in this Section the initial condition is set zero for both the cytokine and the destroyed oligodendrocytes and varies for the macrophages species. We remark that we have also investigated a non zero initial condition for the cytokine species without any qualitatively relevant difference in the resulting outcome. In all the figures showing the spatio-temporal evolution of model (6), we present different snapshots of the apoptotic oligodendrocytes d profile.

6.1 Effects of the aggressiveness r and of the macrophages-driven cytokine production β

We consider the following four scenarios: high aggressiveness (HA) ($r = 6$) and high cytokine production (HcP) ($\beta = 1$); low aggressiveness (LA) ($r = 1$) and high cytokine production (HcP) ($\beta = 1$); high aggressiveness (HA) ($r = 6$) and low cytokine production (LcP) ($\beta = 0.2$); low aggressiveness (LA) ($r = 1$) and low cytokine production (LcP) ($\beta = 0.2$). For all the scenarios, we consider three different chemotaxis values, one below the critical threshold $\chi < \chi_c$, one above the threshold, $\chi > \chi_c$ and one well above criticality $\chi \gg \chi_c$, respectively. All the scenarios are investigated for two different values of the cytokine production rate δ by damaged oligodendrocytes, $\delta = 0$ and $\delta = 1$. The other parameters are fixed as follows: $\epsilon = 0.5, \tau = 1$.

We set a small centered bump (B) as initial condition for the macrophages species, while the cytokine and the damaged oligodendrocytes are initially set to zero. To quantitatively characterize the outcomes of the simulations, for all the four setups we determine the size P_{size} of the plaque (in a sense specified below) and the maximum value M_P assumed by the destroyed oligodendrocytes profile. We remark that all the values reported in the figures and tables refer to the non-dimensional variable $d = \frac{\tilde{d}}{\bar{d}}$. Under the initial macrophages profile chosen, our model produces round-shaped structures in the damaged oligodendrocytes species which maintains the radial symmetry of the macrophages initial profile.

The size P_{size} is computed by measuring the width of the region over which the destroyed oligodendrocytes level decays by a factor e with respect to its peak. This procedure was adopted in [60] to measure the dimensions of Alzheimer senile plaques. Notice that the P_{size} value can decrease in time, in the case when the destroyed oligodendrocytes are rapidly concentrating over a small region. On the other hand, the P_{size} value can also undergo to an abrupt increase when secondary rings form and the damaged oligodendrocytes, here localized, decay by a factor less then e with respect to their peak.

6.1.1 No damaged oligodendrocytes-driven cytokine production ($\delta = 0$)

The HA-HcP scenario is presented in Fig.13 for $\chi = 4, 8, 15$ and $t = 7$ days, being $\chi_c = 5.828$. The time evolutions of P_{size} and M_P are also shown, as well as the slice $d_{sl} = d(\cdot, Y = 1.29\text{cm})$ of the damaged oligodendrocytes at $Y = 1.29$cm at $t = 7$ days. The numerical values of the characteristic quantities P_{size} and M_P at times $t = 2, 4, 6, 7$ are reported in Table 3. We can observe at $t = 7$ that, below the critical threshold

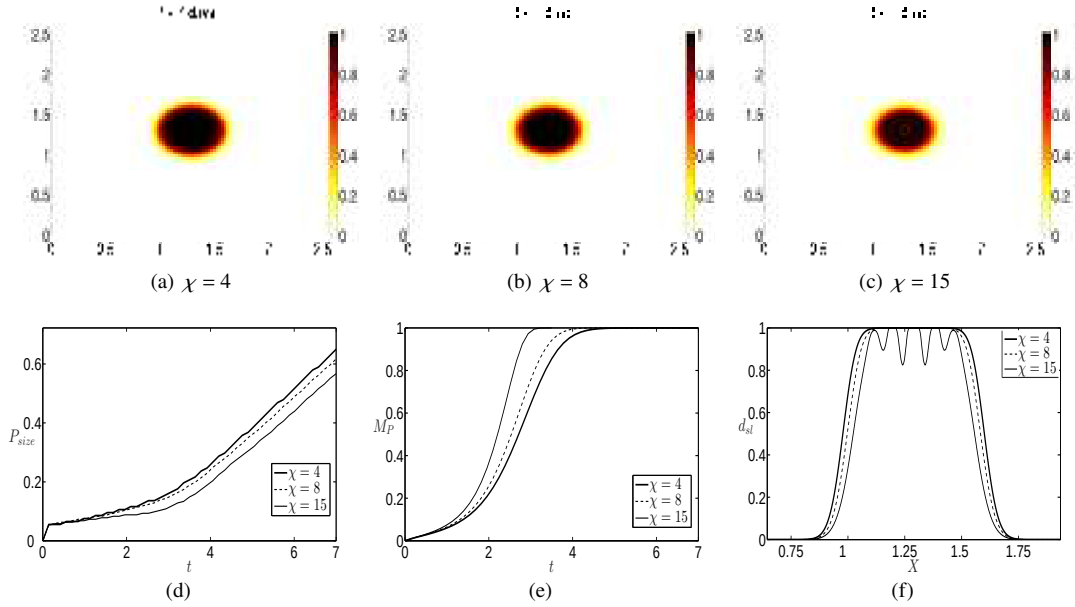

Fig. 13 Sequence of profiles showing the evolution of d (damaged oligodendrocytes) from numerical simulations of model 6 in the case of HA-HcP ($r = 6, \beta = 1$) and $\delta = 0$. The critical chemotaxis value is $\chi_c = 5.828$. The initial condition is B. The plots correspond to the profile of oligodendrocytes at the time $t = 7$ days, for $\chi = 4, 8, 15$ respectively (a-c). (d) Time evolution of the demyelinated plaque diameter P_{size} in the HA-HcP scenario ($r = 6, \beta = 1$) and $\delta = 0$ for different values of χ. (e) Time evolution of the maximum value M_P of the damaged oligodendrocytes species. (f) The slice $d_{sl} = d(\cdot, Y = 1.29\text{cm})$ of the damaged oligodendrocytes at $Y = 1.29$cm at $t = 7$ days for different values of χ

($\chi = 4$) and just above the critical threshold ($\chi = 8$), the destroyed oligodendrocytes form a large homogeneous plaque, whereas well above this threshold ($\chi = 15$) a feeble concentric structure arises. The size P_{size} of the plaque diminishes as χ increases, as a consequence of the increased aggregating strength of the chemotactic term. The maximum value M_P of the destroyed oligodendrocytes increases, at a fixed time, with increasing χ. During the time range $2 < t < 3$ in which M_P has a fast increasing behavior, the P_{size} experiences a small growth rate.

The LA-HcP scenario is presented in Fig.14 for $\chi = 4, 8, 15$ and $t = 7$, being $\chi_c = 5.828$, together with the time evolutions of P_{size}, M_P and the slice $d_{sl} = d(\cdot, Y = 1.29\text{cm})$ of the damaged oligodendrocytes at $t = 7$ days. The corresponding numerical values at times $t = 2, 4, 6, 7$ are reported in Table 3. Similarly to the previous scenario, the size P_{size} of the plaque diminishes as χ increases. We also notice that for $\chi = 15$ this size decreases during the range $2.5 < t < 4$, due to the rapid concentration of the damaged oligodendrocytes in a small central area. In the same case $\chi = 15$, the size of the plaque abruptly increases at $t \approx 5$ and $t \approx 6.6$ due to the formation of two secondary concentric ring. Up to $t = 7$ the concentric structure forms only for $\chi = 15$, while for $\chi = 4, 8$ the damaged oligodendrocytes form a large homogeneous plaque. Due to the smaller aggressiveness, the size of the plaque is lower than the corresponding value in the HA-HcP case for the same value of χ (see Table 3). Moreover, compared to the HA-HcP setup, in the LA-HcP case the concentric rings form in a longer time. However, it is worth noting that, although higher aggressiveness accelerates the formation concentric structures, these structures are more noticeable for lower aggressiveness. In fact, at $t = 7$, the rings are more marked in the LA-HcP case. This can be explained by the fact that an increasing aggressiveness pushes the damaged oligodendrocytes in the central area to the equilibrium value 1, softening the variations between the maxima and the minima that are revealers of the ring appearance. On the other side, by decreasing the aggressiveness, the variations between maxima and minima in the central area are more pronounced and rings are more noticeable.

The HA-LcP scenario for $\chi = 26, 34, 55$ and $t = 7$, being $\chi_c = 29.142$, is presented in Fig.15, where the time evolutions of P_{size}, M_P and the slice $d_{sl} = d(\cdot, Y = 1.29\text{cm})$ of the damaged oligodendrocytes at $t = 7$ days are also shown. The numerical values of P_{size} and M_P at times $t = 2, 4, 6, 7$ are reported in Table 3. Some of the general results already reported in the two previous scenarios are still valid: the size P_{size} of the plaque decreases as χ increases, the maximum value M_P of the destroyed oligodendrocytes increases in time by increasing χ and one can identify a time interval (in this case $3 < t < 5$) during which the P_{size} has a low growth rate. For $\chi = 26, 34$ a large homogeneous plaque forms at $t = 7$, while a concentric structure is

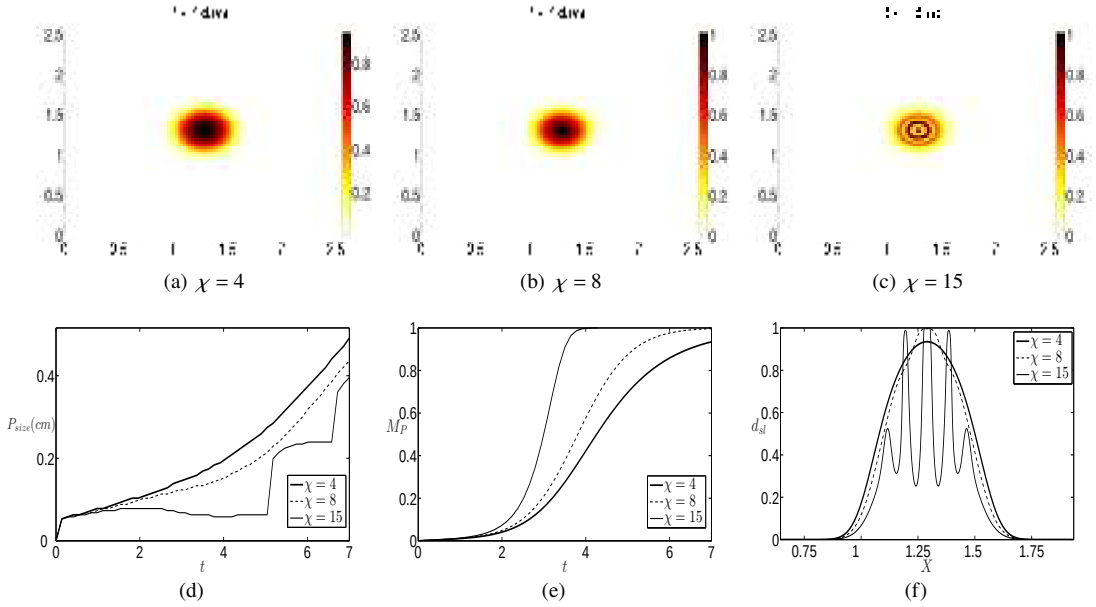

Fig. 14 Sequence of profiles showing the evolution of d (damaged oligodendrocytes) in the case of LA-HcP ($r = 1, \beta = 1$) and $\delta = 0$. The critical chemotaxis value is $\chi_c = 5.828$. The initial condition is B. The plots correspond to the profile of oligodendrocytes at the time $t = 7$ days, for $\chi = 4, 8, 15$ respectively (a-c). (d) Time evolution of the demyelinated plaque diameter P_{size} in the LA-HcP scenario ($r = 1, \beta = 1$) and $\delta = 0$ for different values of χ. (e) Time evolution of the maximum value M_P of the damaged oligodendrocytes species. (f) The slice $d_{sl} = d(\cdot, Y = 1.29\text{cm})$ of the damaged oligodendrocytes at $Y = 1.29$cm at $t = 7$ days for different values of χ

barely visible for $\chi = 55$ (this is almost not observable in Fig.15(c), and it can be better visualized from the d_{sl} profile in Fig.15(f)).

The last LA-LcP scenario is presented in Fig.16 for $\chi = 26, 34, 55$ (being $\chi_c = 29.142$) and $t = 7$ days. The time evolutions of P_{size}, and M_P are also shown in Figs.16 and reported in Table 3, and the the slice $d_{sl} = d(\cdot, Y = 1.29\text{cm})$ of the damaged oligodendrocytes at $t = 7$ days is shown in Fig.16(f). The results are quite similar to the scenario HA-LcP, although, as already observed in the comparison between the scenarios HA-HcP and LA-HcP , the low aggressiveness leads, with respect to the HA-LcP case, to a decreased size of the plaque, to a delay in the time in which the concentric rings form for $\chi = 55$, and to a clearer evidence of the rings structures.

Some general observations can be made from the characterization of the plaques above described in the four scenarios: (i) the size P_{size} of the demyelinated lesion becomes smaller as the chemotactic parameter χ increases (ii) The size P_{size} has lowest growth rate when the maximum value M_P of destroyed oligodendrocytes rapidly increases. (iii) High values of aggressiveness ease the formation of an homogeneous plaque which rapidly tends to the equilibrium value $d = 1$. Moreover, the size P_{size} of the lesion increases with increasing r, as can be seen in Table 3. (iv) For high chemotactic parameter values (well above the critical threshold), an increasing aggressiveness quickens and enhances the formation of concentric rings in the demyelinated lesion, although these concentric structures are more clearly marked for lower aggressiveness. This phenomenon can be easily observed by comparing at $t = 7$ days the HA-HcP with the LA-HcP case for $\chi = 15$, and the HA-LcP with the LA-LcP case for $\chi = 55$ (v) The peak of damaged oligodendrocytes profile increases with both the aggressiveness r and the chemotactic parameter χ.

The above considered four setups do not give an immediate evidence of the effect produced by varying the cytokine production by macrophages on the system dynamics. Hence, we have also performed some numerical simulations by changing the value of β, to determine how this parameters affects the significant features of the lesions. Simulations are performed by fixing $r = 6$, $\delta = 0$, $\epsilon = 0.5$. The chemotactic parameter $\chi = 15$, is in all cases above the critical value, which depends on β. The results are shown in Figs. 17(a)-(c) where we show the time evolutions of the P_{size} and M_P, and the slice $d_{sl} = d(\cdot, Y = 1.29cm)$ of the damaged oligodendrocyte at $Y = 1.29cm$ at $t = 7$ days. Results refer to $\beta = 0.6, 0.8, 1$. We observe that the size P_{size} of the plaque slightly increases as β diminishes. Concentric structure arise only for $\beta = 0.8, 1$. Moreover, an apparent effect of increasing β is to determine the formation of better marked rings of healthy oligodendrocytes (see

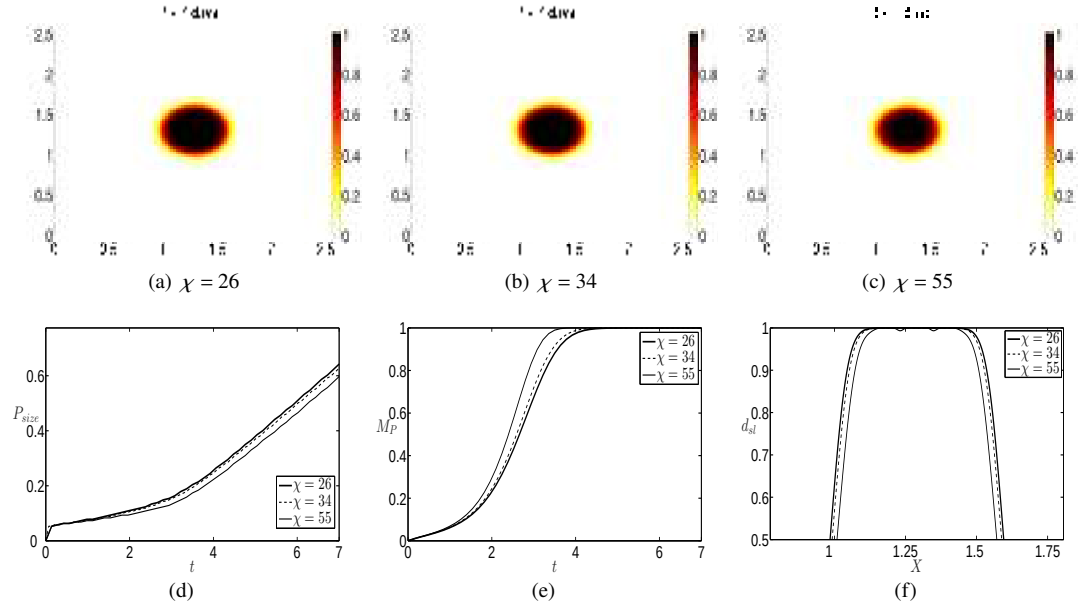

Fig. 15 Sequence of profiles showing the evolution of d (damaged oligodendrocytes) in the case of HA-LcP ($r = 6, \beta = 0.2$) and $\delta = 0$. The critical chemotaxis value is $\chi_c = 29.142$. The initial condition is B. The plots correspond to the profile of oligodendrocytes at the time $t = 7$ days, for $\chi = 26, 34, 55$ respectively (a-c). (d) Time evolution of the demyelinated plaque diameter P_{size} in the HA-LcP scenario ($r = 6, \beta = 0.2$) and $\delta = 0$ for different values of χ. (e) Time evolution of the maximum value M_P of the damaged oligodendrocytes species. (f) The slice $d_{sl} = d(\cdot, Y = 1.29\text{cm})$ of the damaged oligodendrocytes at $Y = 1.29$cm at $t = 7$ days for different values of χ

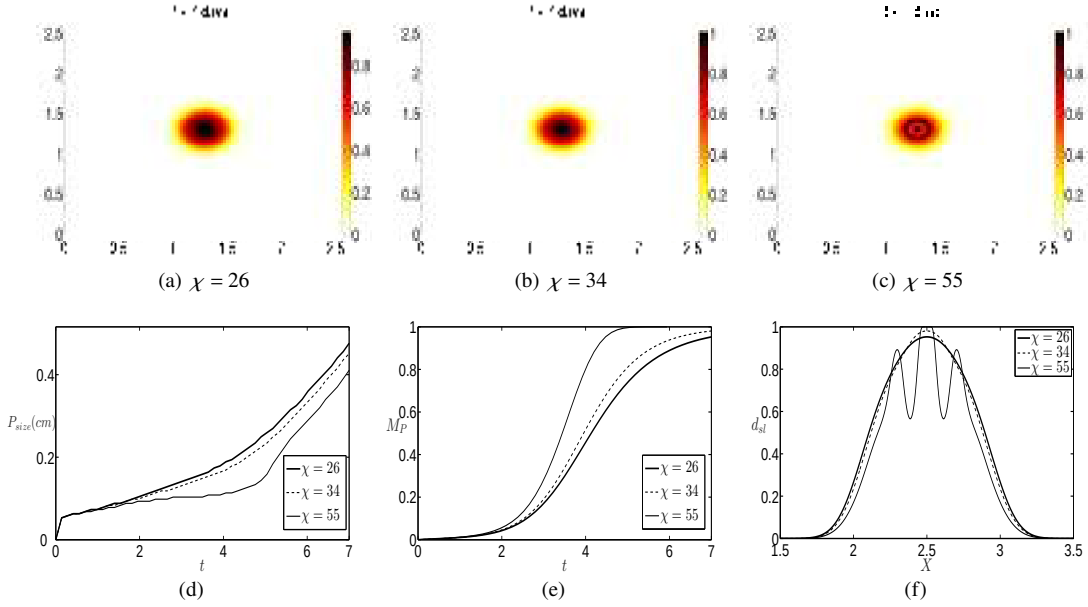

Fig. 16 Sequence of profiles showing the evolution of d (damaged oligodendrocytes) in the case of LA-LcP ($r = 1, \beta = 0.2$) and $\delta = 0$. The critical chemotaxis value is $\chi_c = 29.142$. The initial condition is B. The plots correspond to the profile of oligodendrocytes at the time $t = 7$ days, for $\chi = 26, 34, 55$ respectively (a-c). (d) Time evolution of the demyelinated plaque diameter P_{size} in the LA-LcP scenario ($r = 1, \beta = 0.2$) and $\delta = 0$ for different values of χ. (e) Time evolution of the maximum value M_P of the damaged oligodendrocytes species. (f) The slice $d_{sl} = d(\cdot, Y = 1.29\text{cm})$ of the damaged oligodendrocytes at $Y = 1.29$cm at $t = 7$ days for different values of χ

Fig.17(c)): an analogous effect has already been reported for increasing values of the chemotactic coefficient and decreasing aggressiveness.

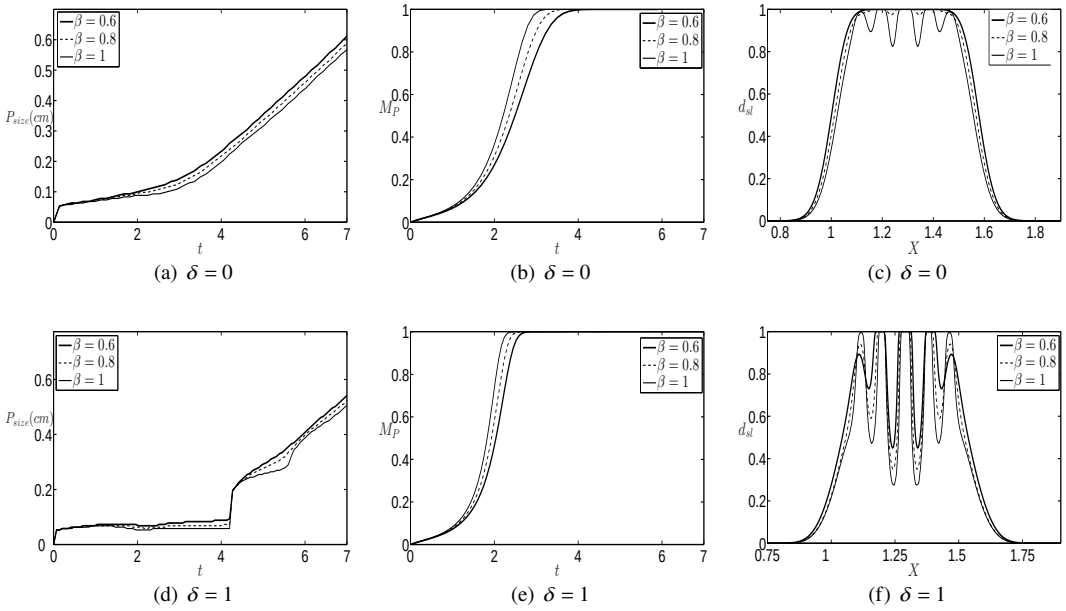

(a) $\delta = 0$ (b) $\delta = 0$ (c) $\delta = 0$

(d) $\delta = 1$ (e) $\delta = 1$ (f) $\delta = 1$

Fig. 17 (a) Time evolution of the demyelinated plaque diameter P_{size} for $r = 1, \epsilon = 0.5, \delta = 0, \chi = 15$ and different βs. (b) Time evolution of the maximum value M_P of the damaged oligodendrocytes species. Parameter are fixed as in (a). (c) The slice $d_{sl} = d(\cdot, Y = 1.259cm)$ of the damaged oligodendrocytes at $Y = 1.29cm$ at $t = 7$ for different values of β. Parameter are fixed as in (a). (d)-(e)-(f) The same as Figs (a)-(b)-(c) but with $\delta = 1$

6.1.2 High damaged oligodendrocytes-driven cytokine production ($\delta = 1$)

The HA-HcP scenario is presented in Fig.18 for $\chi = 4, 8, 15$ and $t = 7$, being $\chi_c = 5.828$, together with the time evolutions of P_{size}, M_P and the slice $d_{sl} = d(\cdot, Y = 1.29\text{cm})$ of the damaged oligodendrocytes at $t = 7$. The numerical values of the characteristic quantities P_{size} and M_P at times $t = 2, 4, 6, 7$ are reported in Table 3. We can observe that below the critical threshold ($\chi = 4$) the destroyed oligodendrocytes form a large homogeneous plaque, whereas above this threshold ($\chi = 8, 15$) a concentric structure arises. As already observed in the case $\delta = 0$, the size P_{size} of the plaque diminishes as χ increases, as a consequence of the increased aggregating strength of the chemotactic term. We also notice that for $\chi = 15$ this size decreases in time in the range $1.51 < t < 2.5$, due to the rapid concentration of the damaged oligodendrocytes in a small central area. The P_{size} abruptly increases after $t = 4$ for the appearance of a secondary concentric ring in which the apoptotic oligodendrocytes value decays by a factor less than e with respect to its peak. The maximum value M_P of the destroyed oligodendrocytes increases with increasing χ. During the time range $1.1 < t < 3$ when M_P has a fast increasing behavior, the P_{size} experiences a small growth rate, which becomes negative in the case $\chi = 15$. Compared with the same scenario in $\delta = 0$ case, we observe that increasing the cytokine production rate by damaged oligodendrocytes, accelerates the phase in which the oligodendrocytes rapidly increase, and favors the formation of concentrating rings which, for $\delta = 1$, are barely visible even for $\chi = 8$. Moreover, comparing the values of P_{size} obtained for $\delta = 0$ and $\delta = 1$ respectively, one can observe that increasing δ has the effect of diminishing the size of the plaque (see Table 3).

In Fig.19 we present the LA-HcP scenario for $\chi = 4, 8, 15$ and $t = 7$ days, being $\chi_c = 5.828$, and the corresponding time evolutions of P_{size}, M_P and the slice $d_{sl} = d(\cdot, Y = 1.29\text{cm})$ of the damaged oligodendrocytes at $t = 7$ days are also shown. The corresponding numerical values P_{size} and M_P at times $t = 2, 4, 6, 7$ are reported in Table 3. The results are similar to those of the scenario HA-HcP. However, due to the reduced aggressiveness, the size of the plaque is smaller than the corresponding value in the HA-HcP case for the same value of χ (see Table 3). Up to $t = 7$ days the concentric structure forms only for values of the chemotaxis coefficient above the critical threshold ($\chi = 8, 15$), while for $\chi = 4$ the damaged oligodendrocytes form a large homogeneous plaque. By comparing this scenario with the same one in the case $\delta = 0$, we deduce, as in the analysis of the previous scenario, that increasing the cytokine production rate by damaged oligodendrocytes eases the formation of concentrating rings.

The HA-LcP scenario is presented in Fig.20 for $\chi = 26, 34, 55$ and $t = 7$ days, being $\chi_c = 29.142$, and the time evolutions of P_{size}, M_P. In the same Figure the slice $d_{sl} = d(\cdot, Y = 1.29\text{cm})$ of the damaged oligodendro-

Table 3 Exact values of P_{size} and M_P at various time for the four scenarios HA-HcP, LA-HcP, HA-LcP, LA-LcP with $\delta = 0$ and $\delta = 1$. Units of measurement are: days for t, and cm for P_{size}. The time evolutions of these quantities are also shown in Figs.13-14-15-16 for $\delta = 0$, and in Figs.18-19-20-21 for $\delta = 1$.

		HA ($r = 6$), HcP ($\beta = 1$) $\chi_c = 5.828$				LA ($r = 1$), HcP ($\beta = 1$) $\chi_c = 5.828$			
		$\delta = 0$		$\delta = 1$		$\delta = 0$		$\delta = 1$	
t (days)	χ	P_{size} (cm)	M_P	P_{size} (cm)	M_P	P_{size} (cm)	M_P	P_{size} (cm)	M_P
2	4	0.108	0.341	0.103	0.401	0.104	0.069	0.106	0.064
4	4	0.258	0.855	0.241	0.951	0.194	0.275	0.179	0.297
6	4	0.516	1	0.493	1	0.377	0.745	0.348	0.815
7	4	0.651	1	0.627	1	0.491	0.934	0.471	0.969
2	8	0.104	0.411	0.082	0.542	0.097	0.085	0.096	0.083
4	8	0.241	0.411	0.185	1	0.155	0.377	0.118	0.473
6	8	0.488	1	0.444	1	0.317	0.919	0.291	0.994
7	8	0.617	1	0.577	1	0.435	0.999	0.411	1
2	15	0.088	0.621	0.052	0.993	0.078	0.015	0.073	0.169
4	15	0.197	1	0.057	1	0.057	0.909	0.042	0.996
6	15	0.438	1	0.387	1	0.238	1	0.214	1
7	15	0.566	1	0.506	1	0.395	1	0.380	1
		HA ($r = 6$), LcP ($\beta = 0.2$) $\chi_c = 5.828$				LA ($r = 1$), LcP ($\beta = 0.2$) $\chi_c = 29.142$			
		$\delta = 0$		$\delta = 1$		$\delta = 0$		$\delta = 1$	
t (days)	χ	P_{size} (cm)	M_P	P_{size} (cm)	M_P	P_{size} (cm)	M_P	P_{size} (cm)	M_P
2	26	0.109	0.361	0.061	0.931	0.104	0.073	0.096	0.082
4	26	0.255	0.881	0.068	1	0.184	0.299	0.093	0.568
6	26	0.508	1	0.382	1	0.357	0.785	0.276	0.999
7	26	0.642	1	0.516	1	0.476	0.952	0.381	1
2	34	0.106	0.363	0.047	0.995	0.097	0.079	0.088	0.098
4	34	0.245	0.916	0.052	1	0.166	0.338	0.063	0.821
6	34	0.498	1	0.259	1	0.332	0.855	0.258	1
7	34	0.627	1	0.471	1	0.451	0.984	0.279	1
2	55	0.094	0.469	0.032	1	0.093	0.099	0.068	0.205
4	55	0.222	0.989	0.032	1	0.111	0.532	0.037	1
6	55	0.464	1	0.224	1	0.287	0.999	0.214	1
7	55	0.597	1	0.395	1	0.410	1	0.375	1

cytes at $t = 7$ days are also shown. The numerical values of P_{size} and M_P at times $t = 2, 4, 6, 7$ are reported in Table 3. The general results already reported in the two previous scenarios are here still valid: the size P_{size} of the plaque decreases as χ increases, the maximum value M_P of the destroyed oligodendrocytes increases in time by increasing χ. In the time interval $2 < t < 3$ the P_{size} diminishes. For all the considered values of χ, the P_{size} abruptly increases after $t = 4$ due to the growing concentric ring. Comparing these results of this scenario with the outcome of the case $\delta = 0$, we observe that for $\delta = 1$ the pattern formation in the damaged oligodendrocytes profile is even more supported, since, for all the considered values of χ, at $t = 7$ days, a concentric ring structure arises.

The last LA-LcP scenario is presented in Fig.21 for $\chi = 26, 34, 55$ and $t = 7$ days, being $\chi_c = 29.142$. The time evolutions of P_{size}, M_P and the slice $d_{sl} = d(\cdot, Y = 1.29\text{cm})$ of the damaged oligodendrocytes at $t = 7$ days are also shown. The numerical values of P_{size} and M_P at times $t = 2, 4, 6, 7$ days are reported in Table 3 . The results are quite similar to the scenario HA-LcP, although, as already observed in the comparison between the scenarios HA-HcP and LA-HcP , the low aggressiveness leads, with respect to the HA-LcP case, to a decreased size of the plaque and to a time delay in the formation of the concentric rings.

A seemingly unexpected phenomenon occurs in the low cytokine production by macrophages and high cytokine production by damaged oligodendrocytes regimes ($\beta = 0.2, \delta = 1$, HA-LcP and LA-LcP): indeed the performed simulations show the formation of concentric structures also for chemotaxis values below the critical threshold. This can of course be motivated by the fact that the chosen initial condition belongs to the basin of attraction of the the pattern found in the simulations shown in Figs.20-21 (a)-(c) and it is not in contrast with the results of the Turing stability analysis below criticality: in fact, we have verified that an initially small perturbation of the uniform equilibrium quickly decays. Furthermore, an initial condition given by a larger bump (about five times larger than the bump assigned above) returns a homogeneous plaque with no ring structures (for brevity the corresponding simulations are not shown here), confirming the expectation that the outcomes of the linear stability analysis are reliable only close to equilibrium.

Summarizing the outcomes of the four setups considered in the high δ regime, we have recovered the qualitative results (i)-(v) deduced from the analysis performed in the case $\delta = 0$. However, for $\delta = 1$, another

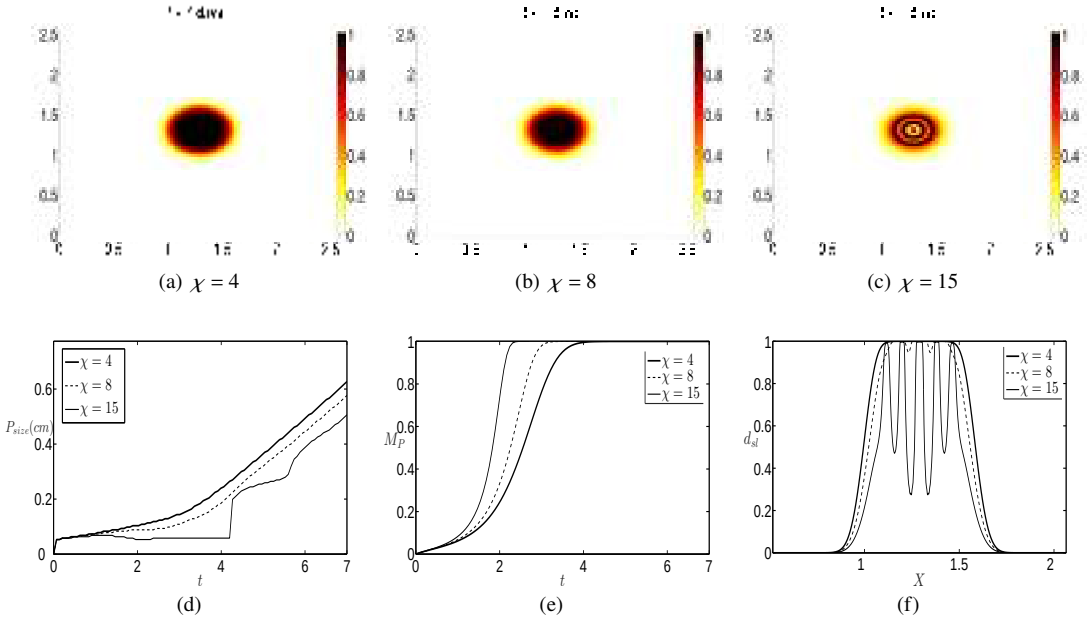

Fig. 18 Sequence of profiles showing the evolution of d (damaged oligodendrocytes) in the case of HA-HcP scenario ($r = 6, \beta = 1$) and $\delta = 1$. The critical chemotaxis value is $\chi_c = 5.828$. The initial condition is B. The plots correspond to the profile of oligodendrocytes at the time step $t = 7$ days, for $\chi = 4, 8, 15$ respectively (a-c). (d) Time evolution of the demyelinated plaque diameter P_{size} for the HA-HcP scenario ($r = 6, \beta = 1$) and $\delta = 1$. (e) Time evolution of the maximum value M_P of the damaged oligodendrocytes species. (f) The slice $d_{sl} = d(\cdot, Y = 1.259cm)$ of the damaged oligodendrocytes at $Y = 1.29cm$ at $t = 7$ days for different values of χ

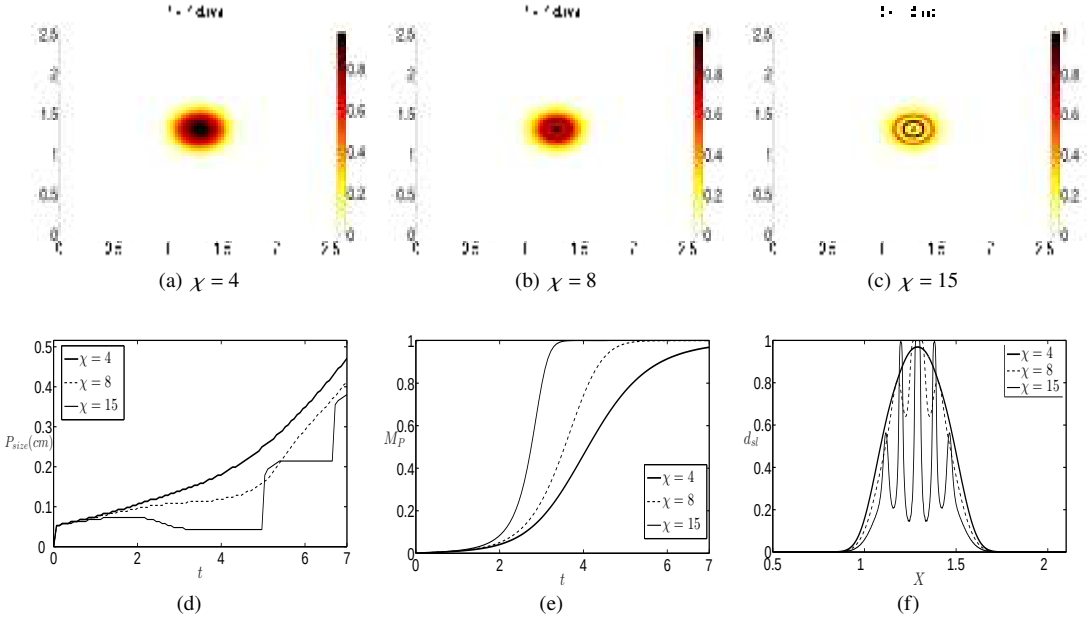

Fig. 19 Sequence of profiles showing the evolution of d (damaged oligodendrocytes) in the case of LA-HcP scenario ($r = 1, \beta = 1$) and $\delta = 1$. The critical chemotaxis value is $\chi_c = 5.828$. The initial condition is B. The plots correspond to the profile of oligodendrocytes at the time step $t = 7$ days, for $\chi = 4, 8, 15$ respectively (a-c). (d) Time evolution of the demyelinated plaque diameter P_{size} for the LA-HcP scenario ($r = 1, \beta = 1$) and $\delta = 1$. (e) Time evolution of the maximum value M_P of the damaged oligodendrocytes species. (f) The slice $d_{sl} = d(\cdot, Y = 1.29cm)$ of the damaged oligodendrocytes at $Y = 1.29cm$ at $t = 7$ days for different values of χ

aspect due to the variation of the parameter χ is better highlighted. In fact, in the case when a concentric

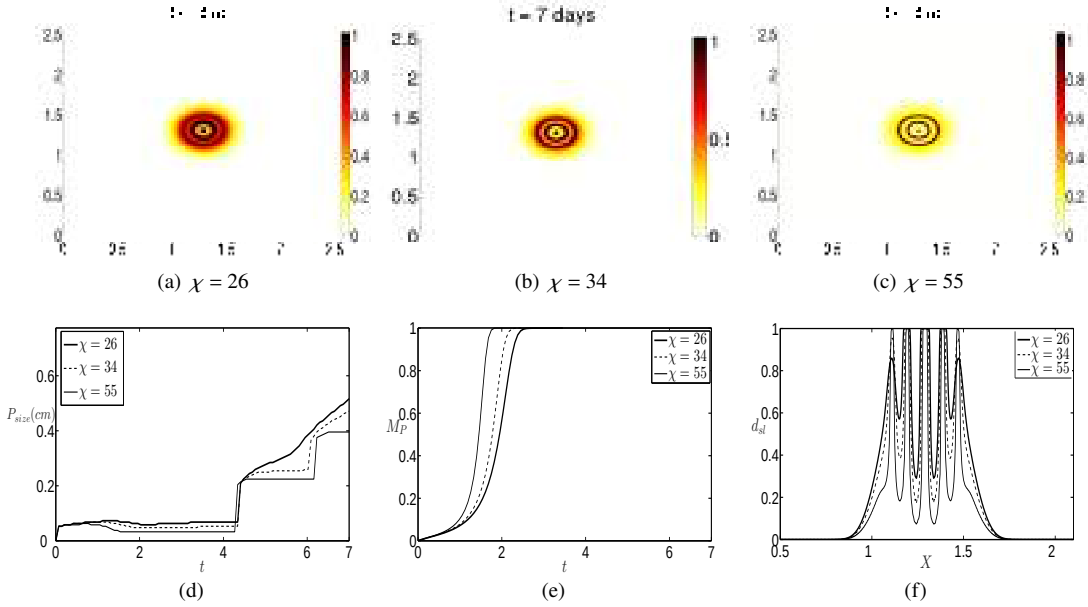

Fig. 20 Sequence of profiles showing the evolution of d (damaged oligodendrocytes) in the case of HA-LcP scenario ($r = 6, \beta = 0.2$) and $\delta = 1$. The critical chemotaxis value is $\chi_c = 29.142$. The initial condition is B. The plots correspond to the profile of oligodendrocytes at the time step $t = 7$ days, for $\chi = 26, 34, 55$ respectively (a-c). (d) Time evolution of the size P_{size} of demyelinated plaque for the HA-LcP scenario ($r = 6, \beta = 0.2$) and $\delta = 1$. (e) Time evolution of the maximum value M_P of the damaged oligodendrocytes species. (f) The slice $d_{sl} = d(\cdot, Y = 1.249cm)$ of the damaged oligodendrocyte at $Y = 1.249cm$ at $t = 7$ days for different values of χ

pattern is formed, as the value of χ is increased the minima of the profile of the apoptotic oligodendrocytes get closer to zero. Therefore, a strong aggregation force close to the sites of high density of activated microglia protects the surroundings, determining the formation of well delimited zones of healthy oligodendrocytes. This phenomenon can be clearly observed in Figs.20(f)-21(f) in the low β regime, whereas it is less evident for high β values (Fig.18(f) and Fig.19(f)), because of the low value of χ above threshold chosen.

To gain a better understanding of the effect of changing the parameter β on the model dynamics, we have performed numerical simulations as β is varied also for the present case $\delta = 1$. Parameter are fixed at $r = 6$, $\delta = 1$, $\epsilon = 0.5$ and $\chi = 15$ (in all cases above the critical threshold). The results are shown in Figs. 17(d)-(f) where we show the time evolutions of the P_{size} and M_P, and the slice $d_{sl} = d(\cdot, Y = 1.249cm)$ of the damaged oligodendrocyte at $Y = 1.249cm$ at $t = 7$ days. Results refer to $\beta = 0.6, 0.8, 1$. We can deduce from the outcomes of the simulations the general results already observed in the case $\delta = 0$. In fact, the size P_{size} of the plaque slightly increases as β diminishes. However, due to the higher cytokine production rate per oligodendrocyte, we observe that for $\delta = 1$ the concentric structures arise for all the β considered, and in the time range $2 < t < 2.5$ the damaged oligodendrocytes rapidly concentrates in a small central area, leading to the decrease of the P_{size}.

6.1.3 Comparing the low and high δ regimes

We conclude this Subsection by discussing the main effects related to the variation of the cytokine production rate δ per oligodendrocyte. We remark the fact that no experimentally measured value of the parameter δ is found in the previous literature. Therefore we have investigated the outcomes supported by the proposed model considering two different schemes: a complete absence of cytokine production by oligodendrocytes ($\delta = 0$), and a relatively high value of it ($\delta = 1$), recording the corresponding effects on the relevant features of the lesions. The conclusions are deduced by comparing the various scenarios for the two different cases $\delta = 0$ and $\delta = 1$, and can be formulated as follows:

(i) A high value of δ eases the formation of concentric structures in the damaged oligodendrocytes profile. In fact, for all the scenarios in the case $\delta = 1$, the concentric rings form for all the chemotaxis values above the critical value χ_c, while for $\delta = 0$ they form only well above χ_c or they form after the final time $t = 7$ days we have considered in our simulations.

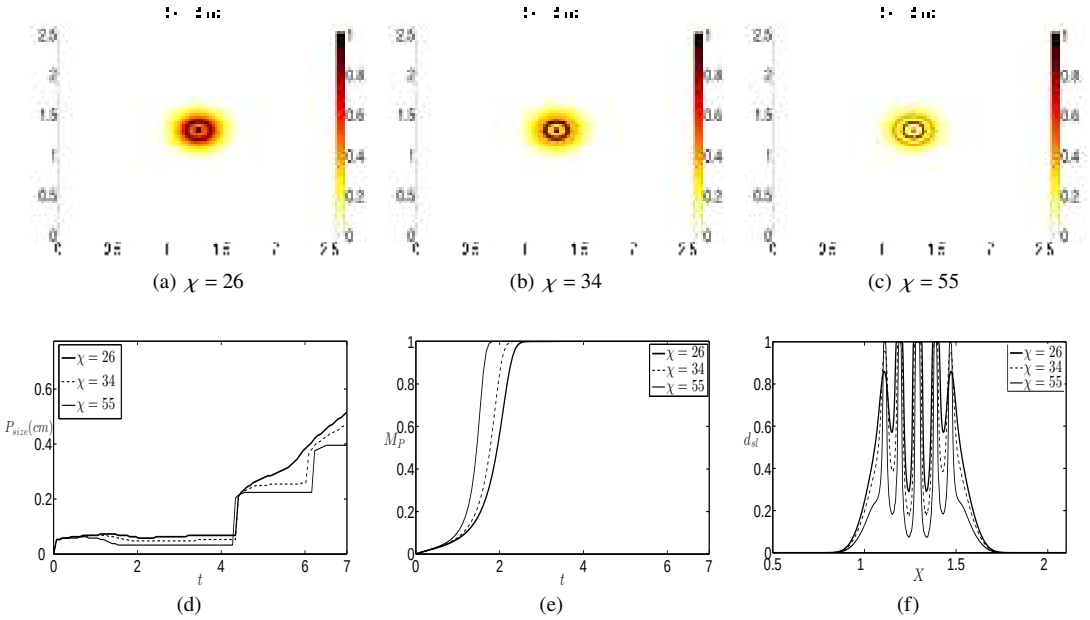

Fig. 21 Sequence of profiles showing the evolution of d (damaged oligodendrocytes) in the case of LA-LcP scenario ($r = 1, \beta = 0.2$) and $\delta = 1$. The critical chemotaxis value is $\chi_c = 29.1428$. The initial condition is B. The plots correspond to the profile of oligodendrocytes at the time step $t = 7$ days, for $\chi = 26, 34, 55$ respectively (a-c). (d) Time evolution of the size P_{size} of demyelinated plaque for the HA-LcP scenario ($r = 1, \beta = 0.2$) and $\delta = 1$. (e) Time evolution of the maximum value M_P of the damaged oligodendrocytes species. (f) The slice $d_{sl} = d(\cdot, Y = 1.29cm)$ of the damaged oligodendrocyte at $Y = 1.29cm$ at $t = 7$ days for different values of χ

(ii) The formed rings are better marked for increasing δ. This can be seen, for instance, by comparing the damaged oligodendrocytes profiles in Figs.15(c),20(c) and in Figs.16(c),21(c).

(iii) The size P_{size} of the plaque increases by diminishing the parameter δ (this can be deduced from the values reported in Table 3)

It is worth noting that the results of the simulations performed by imposing $\delta = 0$ clearly support the fact that the formation of concentric structures above criticality does not depend on the presence of the kinetic term δd in the cytokine dynamics. In effect, this is confirmed by the resultants of the Turing stability analysis shown in Section 3, from which one can clearly see that the conditions for diffusion driven instability only depend on the parameters ϵ and β, whose experimental values are easily found in the existing literature.

6.2 Effects of the cytokine diffusivity coefficient ϵ

To investigate the effect of varying the diffusivity of the cytokine species on the lesions, we consider here the HA-HcP scenario ($r = 6, \beta = 1$) for both the cases $\delta = 0$ and $\delta = 1$, and vary the diffusivity ϵ in the range from 0.6 to 1.5. Moreover, we fix $\tau = 1$ and the chemotaxis value at $\chi = 15$. The critical threshold χ_c increases with ϵ and varies in the range $[6.298, 9.899]$. The chosen initial condition is a small centered bump for the macrophages species (initial condition B), and zero density for both cytokines and apoptotic oligodendrocytes.

In Figs.22-23 we show the damaged oligodendrocytes profiles for $\epsilon = 0.8, 1, 1.5$ at $t = 7$ days in the case $\delta = 0$ and $\delta = 1$, respectively. The case $\epsilon = 0.5$ has been already presented in Figs.13(c)-Figs.18(c). In Figs.22-23 we also show the time evolution of P_{size} and M_P, and the slice $d_{sl} = d(\cdot, Y = 2.5\text{cm})$ of the damaged oligodendrocytes for $Y = 1.249$cm at $t = 7$ days for $\epsilon = 0.6, 0.8, 1, 1.5$.

Since the chemotaxis parameter is above the critical threshold, in all cases concentric structures appear (more marked for $\delta = 1$). One can observe in Figs.22-23(d)-(f) that the P_{size} of the plaque increases with ϵ at least up to time $t \approx 5$, when P_{size} begins to be affected by the presence of the concentric structures. However, the form of the graphs of P_{size} vs t and of M_P vs t show the same qualitative behavior observed in the previous Subsections. Here we just stress a sharper profile of the rings for decreasing ϵ, being the minima of the profile of the apoptotic oligodendrocytes closer to zero as ϵ is decreased.

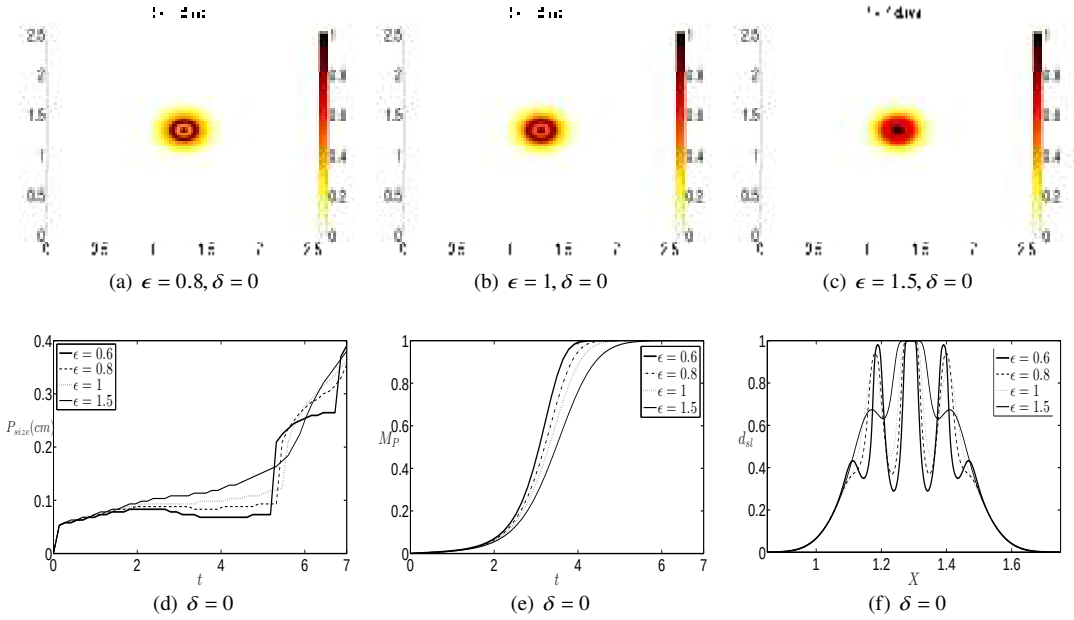

(a) $\epsilon = 0.8, \delta = 0$ (b) $\epsilon = 1, \delta = 0$ (c) $\epsilon = 1.5, \delta = 0$

(d) $\delta = 0$ (e) $\delta = 0$ (f) $\delta = 0$

Fig. 22 Sequence of profiles showing the evolution of d (damaged oligodendrocytes) in the case of HA-HcP ($r = 6, \beta = 1$) for $\delta = 0$. The chemotaxis parameter is fixed at the value $\chi = 15$. The initial condition is B. The plots correspond to the profile of oligodendrocytes at the time step $t = 7$ days, respectively for $\epsilon = 0.8, 1, 1.5$. The profile for $\epsilon = 0.5$ is shown in Fig.13(c). (d) Time evolutions of the size P_{size} of demyelinated plaque in the HA-HcP scenario for different values of ϵ. (e) Time evolutions of the maximum value M_P of the damaged oligodendrocytes species. (f) The slice $d_{sl} = d(\cdot, Y = 2.5\text{cm})$ of the damaged oligodendrocytes at $Y = 2.5$cm at $t = 7$ days for different values of ϵ

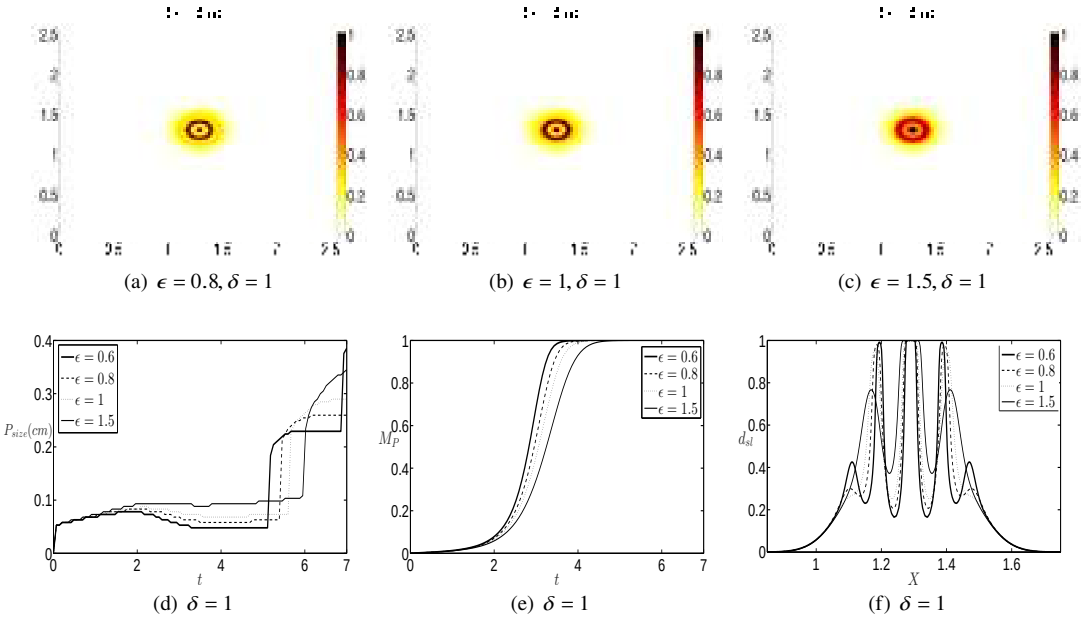

(a) $\epsilon = 0.8, \delta = 1$ (b) $\epsilon = 1, \delta = 1$ (c) $\epsilon = 1.5, \delta = 1$

(d) $\delta = 1$ (e) $\delta = 1$ (f) $\delta = 1$

Fig. 23 Sequence of profiles showing the evolution of d (damaged oligodendrocytes) in the case of HA-HcP ($r = 6, \beta = 1$) for $\delta = 1$. The chemotaxis parameter is fixed at the value $\chi = 15$. The initial condition is B. The plots correspond to the profile of oligodendrocytes at the time step $t = 7$ days, respectively for $\epsilon = 0.8, 1, 1.5$. The profile for $\epsilon = 0.5$ is shown in Fig.18(f). (d) Time evolutions of the size P_{size} of demyelinated plaque in the HA-HcP scenario for different values of ϵ. (e) Time evolutions of the maximum value M_P of the damaged oligodendrocytes species. (f) The slice $d_{sl} = d(\cdot, Y = 1.29\text{cm})$ of the damaged oligodendrocytes at $Y = 1.29$cm at $t = 7$ days for different values of ϵ

6.3 Confluent plaques

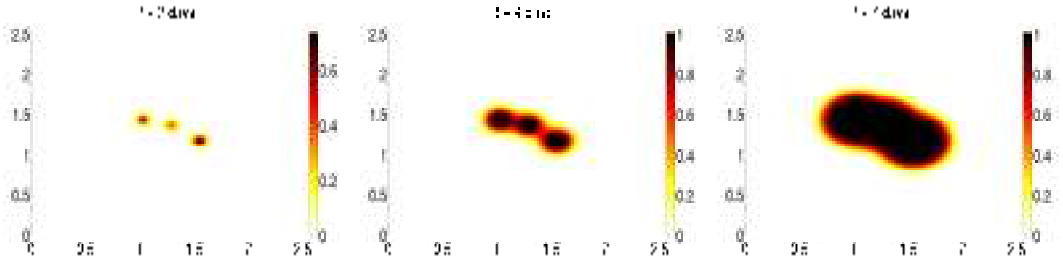

(a) (b) (c)

Fig. 24 Sequence of profiles showing the evolution of d (damaged oligodendrocytes) at various time. The initial condition is given by three small perturbed bumps with different concentration for m and $c = d = 0$. Parameters are $\chi = 4, r = 6, \epsilon = 0.5, \tau = 1, \delta = 0, \beta = 1$

The simulation presented in Fig.24 shows the coalescence of three distinct initial spots of activated macrophages with different size and concentration in the HA-HcP scenario with $\delta = 0$ and $\chi = 4$. One can observe that at $t = 7$ days the spots merge together into a single oblong plaque whose linear size is about 0.9cm. We have found a very similar results for the case $\delta = 1$ (not reported here), in terms of both final plaque structure and length of the plaque. Hence, depending on the location of the initial plaques, one can either observe different homogeneous areas of destroyed oligodendrocytes or the merging of multifocal damaged areas into a single plaque (Fig.24). The latter situation is frequently observed in Multiple Sclerosis pathology, often characterized by the presence of confluent subpial cortical lesions. Note that the chosen parameter set is such that the chemotactic parameter is below the instability threshold and no ring structures arise.

6.4 Clusters of activated microglia: pre-active lesions

In this Subsection we examine the spatio-temporal evolution originated by a spatially distributed small random perturbation of the macrophages density and zero initial condition for both the cytokines and the damaged oligodendrocytes.

The profiles of the activated macrophages and apoptotic oligodendrocytes shown in Figs. 25 are the outcomes of a simulation with low aggressiveness ($r = 0.01$), moderate-low diffusivity ($\epsilon = 0.5$), high cytokine production by macrophages ($\beta = 1$), absence of cytokine production by damaged oligodendrocytes ($\delta = 0$), and a chemotactic parameter $\chi = 20$ above the critical threshold.

We have performed some numerical simulations for the same parameter set, varying the parameter δ, without noticing any relevant difference in the species densities.

In Fig. 25 we observe the formation of small high density clusters of activated macrophages all over the domain followed by the appearance of scarcely populated aggregates of damaged oligodendrocytes.

The reported pattern reproduces some experimental findings observed in the so-called pre-active lesions, round or oval regions whose key feature is the presence of clusters (nodules) of activated microglia in absence of demyelination, observed in the majority of Multiple Sclerosis patients [23, 43]. Preactive lesions are not associated with blood vessel and their exact size is considered a nondiscriminatory variable [88]. According to a well-accepted scenario of lesion development, pre-active lesions are considered the first specific signs of reversible early disorder, preceding the onset of the classical inflammatory lesions typified by myelin degradation. In fact, in most cases the activation of microglia resolves with time and only a few of the pre-active lesions lead to the development of actively demylinating plaques. This could be caused by natural neuroprotective mechanisms induced by activated microglia which, if on the one side actively contribute to tissue destruction and neurodegeneration, on the other side play a key role in endogenous neuroprotective pathways releasing neurotrophic factors and immunomodulatory molecules [76]. In-depth analysis of the mechanisms involved in creating pre-active lesions and how they progress to a destructive state would therefore offer novel clues for modeling and for the design of neuroprotective therapeutic strategies [74].

The above presented numerical results, together with those shown in the previous Subsections, are in good agreement with some of the experimental observations found in literature, both for the shape of the lesions,

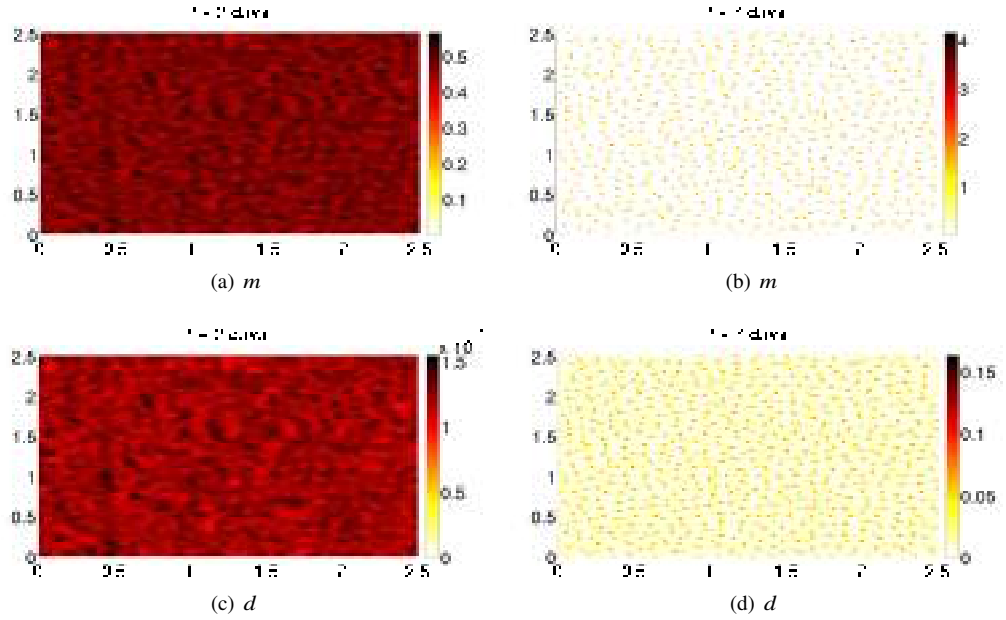

(a) m (b) m

(c) d (d) d

Fig. 25 Spatial distribution of m (activated macrophages) and d (damage oligodendrocytes) at different times. The initial condition is a random noise all over the domain for m and $c = d = 0$. Parameters are $r = 0.01, \epsilon = 0.5, \beta = 1, \tau = 1, \delta = 0$, and $\chi = 20$

which is typically spherical or ovoidal (see [16, 86]), for the time evolution of the spots (see [36, 68]) and for the size. On the other hand it has to be stressed that the MRI of patients affected by MS demonstrate the presence of lesions with an high variability in the linear size, which can range from few millimeters to centimeters ([86]).

7 Comparison with the Khonsari-Calvez model of Baló's sclerosis

In this section we provide a detailed comparison between Baló's multiple sclerosis model introduced by Calvez and Khonsari [15, 48] and the model proposed here and expressed by (6). The two models provide a relevant framework for reproducing the leading mechanisms describing the demyelination process common in the neuropathology of multiple sclerosis subtypes.

The system (6) proposed in this paper shares with the Kohnsari-Calvez model the description of the self organization mechanisms based on the chemotactic motion of cells together with activation and propagation.

The aim, here, is to explore a wider spectrum of scenarios, within the experimentally available ranges of variations of the involved parameters, so to reproduce some of the different pathological features observed in the various subtypes of MS.

A first difference involves the kinetics of cytokine: differently from what assumed in [48], on the basis of the known immunological pathways, we added an additional term describing the production of the chemical signal by macrophages. The simulations show that the presence of this term has the effect to ease the aggregation of macrophages species: we observe the formation of lesions and a time evolution towards stabilization compatible with measured times. On the other hand, in the simulations performed by Khonsari-Calvez (see [48]), one can observe a quick saturation and the formation of homogeneous plaques in a short timescale. Indeed, in the presence of a non-zero production of pro-inflammatory cytokines by activated macrophages, the formation of the aggregates occurs also if there is no cytokine production by apoptotic oligodendrocytes, an effect which is the key mechanism in [48].

Furthermore, we opted for a parabolic equation for the cytokine species, introducing the parameter τ, which measures the characteristic time-scale of their evolution. This allows one to investigate different dynamical behaviors as τ is varied and to get the quasi-steady state approximation adopted in [48] in the limit of $\tau \to 0$.

Another difference with K-C model concerns the functional form of the sensitivity function in the chemotactic term. To avoid unrealistic cell overcrowding which contrasts with the finite size of individual cells and the behavior of cells at higher densities, in K-C model the non linear diffusion term is expressed by a saturating

term which has a degeneration for $m = 1$. We propose a biologically equivalent expression for the saturation of macrophages which in turn removes this singularity and makes the mathematical investigation easier.

We have performed some numerical investigation to compare the outcomes prescribed by the two models under the same conditions. The numerical results shown in Figs.26(a)-(c) are initiated by a small centered bump of activated macrophages. We set the chemotaxis value at $\chi = 30$, above the critical threshold, and the parameters as follows: $\tau = 0.001$, $\beta = 0.2$, $\epsilon = 0.5$, $\delta = 1$, $r = 6$. Thus, one can observe that in the limit of small τ and β, our model has a similar behavior to the one prescribed by [48], i.e. it is able to produce Baló's type concentric damaged areas with thickness $\sim 0.4mm$ at $t = 7$. This thickness does not vary as time progresses ($t = 14$ days). A homogeneous demyelinated plaque occurs for $\chi = 6$, as shown in Figs.26(d)-(e). Therefore, in the limit $\tau, \beta \to 0$, the system (6) shares common qualitative outcomes with the model proposed by Khonsari and Calvez, showing either one of two different scenarios as the parameter χ is varied: very early stages of MS (homogeneous plaque) and concentric lesions of Baló's sclerosis.

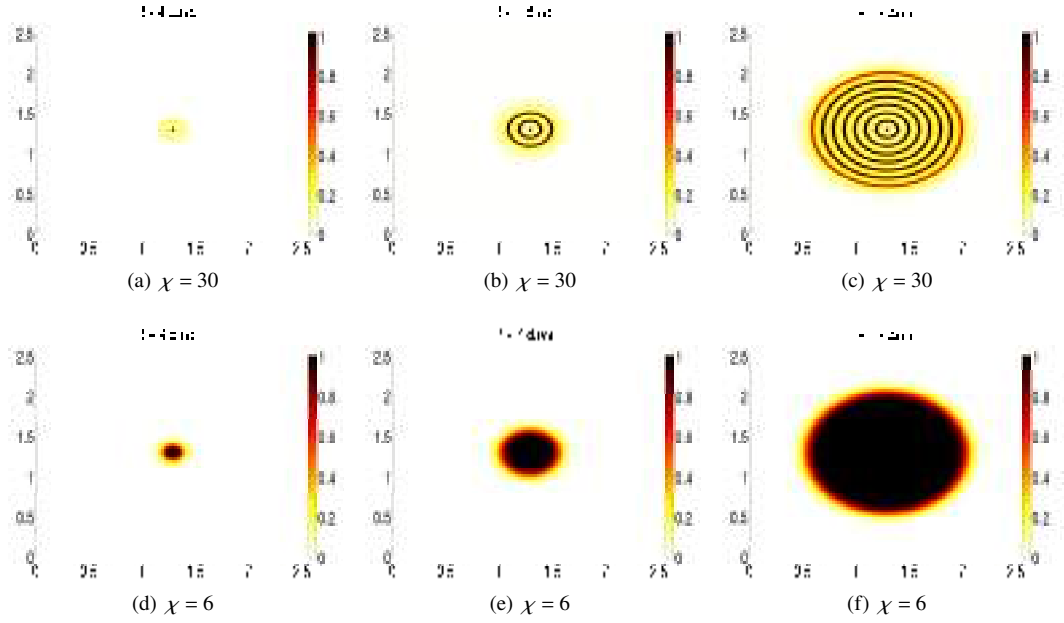

(a) $\chi = 30$ (b) $\chi = 30$ (c) $\chi = 30$

(d) $\chi = 6$ (e) $\chi = 6$ (f) $\chi = 6$

Fig. 26 (a)-(b)-(c) Spatial distribution of d (damage oligodendrocytes) at different times in the HA-HcP set-up for $\chi = 30$. The initial condition is a small centered bump of activated macrophages for m and $c = d = 0$. (d)-(e)-(f) Damaged oligodendrocytes profile at different times for $\chi = 6$. In both the simulations, parameters are: $\tau = 0.001$, $\beta = 0.2$, $\epsilon = 0.5$, $\delta = 1$, $r = 6$

8 Conclusions

According to the current consensus, the pathogenesis of the MS lesion is heterogeneous and no single predominant mechanism for demyelination and neurodegeneration has emerged. In this paper we have proposed a mathematical model which reproduces the molecular processes involved in the genesis of type III lesions, which are also believed to be effective in the early stages of tissue injury, which precedes the formation of hypoxia-like demyelinated plaques. Despite this heterogeneity and the several complex biological phenomena involved in the disease, here we focused our attention only on oligodendrocytes apoptosis and macrophages activation, mainly due to an autoimmune inflammatory mechanism.

On 1D domains the model supports the formation of stationary patterns close to the Turing bifurcation threshold and shows the emergence of complex oscillatory solutions far from equilibrium. On 2D domains one observes the appearance of localized spots of apoptotic oligodendrocytes areas, whose size is regulated by the phagocytosis aggressiveness of the macrophages and by the diffusivity of the cytokines. Indeed a comparison between some MRI data ([16, 36, 86]) and our numerical simulations has revealed a good agreement with the size and shape of the plaques observed in clinical cases. Moreover, in accordance with the fact that the dimension of a new plaque is well defined within few days after initial symptoms [2], the time scale for

the emergence of new lesions and the linear dimensions observed in our results are compatible with the experimental data.

Although the model proposed here describes the subtype III lesions of MS, it is also able to reproduce Baló's sclerosis demyelinated rings, the formation of confluent plaques and the neuropathological state characterized by the presence of nodules of activated macrophages, observed in the reversible first stages of MS.

The numerical simulations performed here have some limitations due to the heterogeneous composition of the white matter of the brain: since lesions are frequently clustered around the periventricular white matter, the main improvement in this direction should be the inclusion of the four cerebral ventricles in order to obtain a more realistic 2D domain. This could also be accomplished utilizing a mesh-free algorithm based on particle methods [5, 20, 24] which has proven to be effective in the study of reaction-diffusion systems in presence of nonlinear diffusion terms [29, 30].

It is well known that cytokine has both the roles of promoting and contrasting inflammation. As suggested by some models of inflammatory diseases ([27, 37, 38, 60, 77]), a possible modeling improvement could be to take into account the presence of an inhibitory cytokine, here neglected, and investigate the possible effects of this anti-inflammatory component not only on the formation and evolution of the lesions but also on the onset of reparative effects leading to remyelination [9]. Indeed, remyelination is a common phenomenon in Multiple Sclerosis: oligodendrocyte precursor cells can be recruited and reappear in inactive plaque centers. The arising remyelinated areas, the so-called shadow plaques, are then characterized by thin irregular shaped myelin sheaths within the whole lesion. These shadow plaques are present in lesions of I and II subtypes, whereas rarely observed in chronic MS lesions of III and IV subtypes [62], their presence certainly depending on the availability of oligodendrocyte precursor cells and the pro and anti inflammatory balance [80].

From a mathematical point of view, it would be of interest to derive the explicit form and the amplitude of the resulting patterns close to bifurcation through a weakly nonlinear analysis in the case of 2D domains [11, 22, 32, 34]. This will be the subject of a forthcoming paper.

One could also consider the inclusion of nonlinear diffusion terms ([33, 34, 65, 85]) and investigate the effects on the phenomenon of plaque formation. In particular the presence of a nonlinear self diffusion term of the type introduced in [34, 51] could be used to quantitatively explore the stimulated migratory response of macrophages through 3D fibrin gels, which in recent years have been employed to realistically model macrophage migration [69].

Some attention could be devoted to the study of far from equilibrium phenomena. This should include the analysis of complex spatio-temporal patterning on the 1D domain, such as stationary periodic, oscillatory and chaotic dynamics, which has also been recently found in the Keller-Segel system with logistic growth [41, 75].

Also the presence of localized dissipative structures such as spikes [19, 40, 45, 89], bubbles [54], hotspots [49], and their stability has been the object of extensive investigations in many recent papers. The exploration of similar dynamics in this case could shed more lights on the mechanisms underling the demyelinating patterns.

Moreover, it could be worth studying the nonlinear stability of system (6) using a suitable Lyapunov functional or adopting a proper reduction method (see [70]).

Finally, it would be of interest to explore some discrete approach to the simulation of the processes involved in the evolution of MS: agent-based modeling and cellular automata offer a way to model complex adaptive system characterized by emergent order and self-organization and have been successfully applied for the description of related phenomena [6–8, 78].

Acknowledgements

The work of the second author (RB) has been supported by INDAM-GNFM through a *Progetto giovani* grant. The authors gratefully thank two anonymous reviewers for their suggestions and comments which have significantly helped in improving the presentation of the paper.

References

1. Banati, R.B., Newcombe, J., Gunn, R.N., Cagnin, A., Turkheimer, F., Heppner, F., Price, G., Wegner, F., Giovannoni, G., Miller, D.H., Perkin, G.D., Smith, T., Hewson, A.K., Bydder, G., Kreutzberg, G.W., Jones, T., Cuzner, M.L., Myers, R.: The peripheral benzodiazepine binding site in the brain in multiple sclerosis. Brain **123**(11), 2321–2337 (2000)
2. Barnett, M., Prineas, J.: Relapsing and remitting multiple sclerosis: Pathology of the newly forming lesion. Annals of Neurology **55**(4), 458–468 (2004)

3. Barnett, M.H., Parratt, J.D.E., Pollard, J.D., Prineas, J.W.: MS: Is it one disease? International MS Journal **16**(2), 57–65 (2009)
4. Barresi, R., Bilotta, E., Gargano, F., Lombardo, M., Pantano, P., Sammartino, M.: Wavefront invasion for a chemotaxis model of multiple sclerosis. Ricerche di Matematica pp. 1–12 (2016)
5. Beaudoin, A., Huberson, S., Rivoalen, E.: Simulation of anisotropic diffusion by means of a diffusion velocity method. Journal of Computational Physics **186**(1), 122–135 (2003)
6. Bilotta, E., Pantano, P.: Emergent patterning phenomena in 2D cellular automata. Artificial Life **11**(3), 339–362 (2005)
7. Bilotta, E., Pantano, P.: Artificial micro-worlds part II: Cellular automata growth dynamics. International Journal of Bifurcation and Chaos **21**(3), 619–645 (2011)
8. Bilotta, E., Pantano, P., Vena, S.: Artificial micro-worlds part I: A new approach for studying life-like phenomena. International Journal of Bifurcation and Chaos **21**(2), 373–398 (2011)
9. Bø, L., Esiri, M., Evangelou, N., Kuhlmann, T.: Demyelination and Remyelination in Multiple Sclerosis, pp. XIV, 290. Springer US (2013)
10. Boche, D., Perry, V., Nicoll, J.: Review: Activation patterns of microglia and their identification in the human brain. Neuropathology and Applied Neurobiology **39**(1), 3–18 (2013)
11. Bozzini, B., Gambino, G., Lacitignola, D., Lupo, S., Sammartino, M., Sgura, I.: Weakly nonlinear analysis of Turing patterns in a morphochemical model for metal growth. Computers and Mathematics with Applications **70**(8), 1948–1969 (2015)
12. Breij, E., Brink, B., Veerhuis, R., Van Den Berg, C., Vloet, R., Yan, R., Dijkstra, C., Van Der Valk, P., Bø, L.: Homogeneity of active demyelinating lesions in established multiple sclerosis. Annals of Neurology **63**(1), 16–25 (2008)
13. Burger, M., Di Francesco, M., Dolak-Struss, Y.: The Keller-Segel model for chemotaxis with prevention of overcrowding: Linear vs. nonlinear diffusion. SIAM Journal on Mathematical Analysis **38**(4), 1288–1315 (2006)
14. Calvez, V., Corrias, L.: The parabolic-parabolic Keller-Segel model in $\mathbb{R}^2$. Communications in Mathematical Sciences **6**(2), 417–447 (2008)
15. Calvez, V., Khonsari, R.: Mathematical description of concentric demyelination in the human brain: Self-organization models, from Liesegang rings to chemotaxis. Mathematical and Computer Modelling **47**(7-8), 726–742 (2008)
16. Cerasa, A., Bilotta, E., Augimeri, A., Cherubini, A., Pantano, P., Zito, G., Lanza, P., Valentino, P., Gioia, M., Quattrone, A.: A cellular neural network methodology for the automated segmentation of multiple sclerosis lesions. Journal of Neuroscience Methods **203**(1), 193–199 (2012)
17. Chalmers, A., Cohen, A., Bursill, C., Myerscough, M.: Bifurcation and dynamics in a mathematical model of early atherosclerosis: How acute inflammation drives lesion development. Journal of Mathematical Biology **71**(6-7), 1451–1480 (2015)
18. Chen, C.J., Chu, N.S., Lu, C.S., Sung, C.Y.: Serial magnetic resonance imaging in patients with Balo's concentric sclerosis: Natural history of lesion development. Annals of Neurology **46**(4), 651–656 (1999)
19. Chen, X., Hao, J., Wang, X., Wu, Y., Zhang, Y.: Stability of spiky solution of Keller-Segel's minimal chemotaxis model. Journal of Differential Equations **257**(9), 3102–3134 (2014)
20. Chertock, A., Kurganov, A.: On a practical implementation of particle methods. Applied Numerical Mathematics **56**(10-11 SPEC. ISS.), 1418–1431 (2006)
21. Childress, S., Percus, J.: Nonlinear aspects of chemotaxis. Mathematical Biosciences **56**(3-4), 217–237 (1981)
22. Cruywagen, G., Maini, P., Murray, J.: Biological pattern formation on two-dimensional spatial domains: A nonlinear bifurcation analysis. SIAM Journal on Applied Mathematics **57**(6), 1485–1509 (1997)
23. De Groot, C., Bergers, E., Kamphorst, W., Ravid, R., Polman, C., Barkhof, F., Van Der Valk, P.: Post-mortem mri-guided sampling of multiple sclerosis brain lesions: Increased yield of active demyelinating and (p)reactive lesions. Brain **124**(8), 1635–1645 (2001)
24. Degond, P., Mustieles, F.J.: A deterministic approximation of diffusion equations using particles. SIAM Journal on Scientific and Statistical Computing **11**(2), 293–310 (1990)
25. Dolak, Y., Schmeiser, C.: The Keller-Segel model with logistic sensitivity function and small diffusivity. SIAM Journal on Applied Mathematics **66**(1), 286–308 (2006)
26. Edelstein-Keshet, L., Spiros, A.: Exploring the formation of Alzheimer's disease senile plaques in silico. Journal of Theoretical Biology **216**(3), 301–326 (2002)
27. El Khatib, N., Genieys, S., Kazmierczak, B., Volpert, V.: Reaction-diffusion model of atherosclerosis development. Journal of Mathematical Biology **65**(2), 349–374 (2012)

28. Fischer, M., Wimmer, I., Höftberger, R., Gerlach, S., Haider, L., Zrzavy, T., Hametner, S., Mahad, D., Binder, C., Krumbholz, M., Bauer, J., Bradl, M., Lassmann, H.: Disease-specific molecular events in cortical multiple sclerosis lesions. Brain **136**(6), 1799–1815 (2013)
29. Galiano, G., Selgas, V.: Deterministic particle method approximation of a contact inhibition cross-diffusion problem. Applied Numerical Mathematics **95**, 229 – 237 (2015)
30. Gambino, G., Lombardo, M., Sammartino, M.: A velocity-diffusion method for a Lotka-Volterra system with nonlinear cross and self-diffusion. Applied Numerical Mathematics **59**(5), 1059–1074 (2009)
31. Gambino, G., Lombardo, M., Sammartino, M.: Turing instability and traveling fronts for a nonlinear reaction-diffusion system with cross-diffusion. Mathematics and Computers in Simulation **82**(6), 1112–1132 (2012)
32. Gambino, G., Lombardo, M., Sammartino, M.: Pattern formation driven by cross-diffusion in a 2D domain. Nonlinear Analysis: Real World Applications **14**(3), 1755–1779 (2013)
33. Gambino, G., Lombardo, M., Sammartino, M.: Turing instability and pattern formation for the Lengyel-Epstein system with nonlinear diffusion. Acta Applicandae Mathematicae **132**(1) (2014)
34. Gambino, G., Lombardo, M., Sammartino, M., Sciacca, V.: Turing pattern formation in the Brusselator system with nonlinear diffusion. Physical Review E - Statistical, Nonlinear, and Soft Matter Physics **88**(4) (2013)
35. Goodhill, G.: Diffusion in axon guidance. European Journal of Neuroscience **9**(7), 1414–1421 (1997)
36. Guttmann, C., Ahn, S., Hsu, L., Kikinis, R., Jolesz, F.: The evolution of multiple sclerosis lesions on serial MR. American Journal of Neuroradiology **16**(7), 1481–1491 (1995)
37. Herald, M.: General model of inflammation. Bulletin of Mathematical Biology **72**(4), 765–779 (2010)
38. Hidalgo, A., Tello, L., Toro, E.: Numerical and analytical study of an atherosclerosis inflammatory disease model. Journal of Mathematical Biology **68**(7), 1785–1814 (2014)
39. Hillen, T., Painter, K.: Global existence for a parabolic chemotaxis model with prevention of overcrowding. Advances in Applied Mathematics **26**(4), 280–301 (2001)
40. Hillen, T., Painter, K.J.: A user's guide to PDE models for chemotaxis. Journal of mathematical biology **58**(1-2), 183–217 (2009)
41. Hillen, T., Zielinski, J., Painter, K.: Merging-emerging systems can describe spatio-temporal patterning in a chemotaxis model. Discrete and Continuous Dynamical Systems - Series B **18**(10), 2513–2536 (2013)
42. Hohlfeld, R., Wekerle, H.: Autoimmune concepts of multiple sclerosis as a basis for selective immunotherapy: From pipe dreams to (therapeutic) pipelines. Proceedings of the National Academy of Sciences of the United States of America **101**(SUPPL. 2), 14,599–14,606 (2004)
43. van Horssen, J., Singh, S., van der Pol, S., Kipp, M., Lim, J., Peferoen, L., Gerritsen, W., Kooi, E.J., Witte, M., Geurts, J., de Vries, H., Peferoen-Baert, R., van den Elsen, P., van der Valk, P., Amor, S.: Clusters of activated microglia in normal-appearing white matter show signs of innate immune activation. Journal of Neuroinflammation **9** (2012)
44. Jensen, O., Pannbacker, V., Mosekilde, E., Dewel, G., Borckmans, P.: Localized structures and front propagation in the Lengyel-Epstein model. Physical Review E **50**(2), 736–749 (1994)
45. Kang, K., Kolokolnikov, T., Ward, M.: The stability and dynamics of a spike in the 1d Keller-Segel model. IMA Journal of Applied Mathematics (Institute of Mathematics and Its Applications) **72**(2), 140–162 (2007)
46. Keller, E., Segel, L.: Initiation of slime mold aggregation viewed as an instability. Journal of Theoretical Biology **26**(3), 399–415 (1970)
47. Keller, E., Segel, L.: Model for chemotaxis. Journal of Theoretical Biology **30**(2), 225–234 (1971)
48. Khonsari, R., Calvez, V.: The origins of concentric demyelination: Self-organization in the human brain. PLoS ONE **2**(1) (2007)
49. Kolokolnikov, T., Ward, M., Wei, J.: The stability of steady-state hot-spot patterns for a reaction-diffusion model of urban crime. Discrete and Continuous Dynamical Systems - Series B **19**(5), 1373–1410 (2014)
50. Kolokolnikov, T., Wei, J., Alcolado, A.: Basic mechanisms driving complex spike dynamics in a chemotaxis model with logistic growth. SIAM Journal on Applied Mathematics **74**(5), 1375–1396 (2014)
51. Kumar, N., Horsthemke, W.: Turing bifurcation in a reaction-diffusion system with density-dependent dispersal. Physica A: Statistical Mechanics and its Applications **389**(9), 1812 – 1818 (2010)
52. Kumar, R., Clermont, G., Vodovotz, Y., Chow, C.: The dynamics of acute inflammation. Journal of Theoretical Biology **230**(2), 145–155 (2004)
53. Kutzelnigg, A., Lassmann, H.: Chapter 2 - Pathology of multiple sclerosis and related inflammatory demyelinating diseases. In: Goodin, D.S. (ed.) Multiple Sclerosis and Related Disorders, *Handbook of Clinical Neurology*, vol. 122, pp. 15 – 58. Elsevier (2014)

54. Lai, X., Chen, X., Wang, M., Qin, C., Zhang, Y.: Existence, uniqueness, and stability of bubble solutions of a chemotaxis model. Discrete and Continuous Dynamical Systems- Series A **36**(2), 805–832 (2016)
55. Lassmann, H.: Multiple sclerosis pathology: Evolution of pathogenetic concepts. Brain Pathology **15**(3), 217–222 (2005)
56. Lassmann, H.: Review: The architecture of inflammatory demyelinating lesions: Implications for studies on pathogenesis. Neuropathology and Applied Neurobiology **37**(7), 698–710 (2011)
57. Lassmann, H., Niedobitek, G., Aloisi, F., Middeldorp, J.: Epstein-barr virus in the multiple sclerosis brain: A controversial issue-report on a focused workshop held in the centre for brain research of the medical university of vienna, austria. Brain **134**(9), 2772–2786 (2011)
58. Lassmann, H., Van Horssen, J.: The molecular basis of neurodegeneration in multiple sclerosis. FEBS Letters **585**(23), 3715–3723 (2011)
59. Lee, S., Liu, W., Dickson, D., Brosnan, C., Berman, J.: Cytokine production by human fetal microglia and astrocytes: Differential induction by lipopolysaccharide and il-1β. Journal of Immunology **150**(7), 2659–2667 (1993)
60. Luca, M., Chavez-Ross, A., Edelstein-Keshet, L., Mogilner, A.: Chemotactic signaling, microglia, and Alzheimer's disease senile plaques: Is there a connection? Bulletin of Mathematical Biology **65**(4), 693–730 (2003)
61. Lucchinetti, C., Brück, W., Parisi, J., Scheithauer, B., Rodriguez, M., Lassmann, H.: A quantitative analysis of oligodendrocytes in multiple sclerosis lesions. a study of 113 cases. Brain **122**(12), 2279–2295 (1999)
62. Lucchinetti, C., Brück, W., Parisi, J., Scheithauer, B., Rodriguez, M., Lassmann, H.: Heterogeneity of multiple sclerosis lesions: Implications for the pathogenesis of demyelination. Annals of Neurology **47**(6), 707–717 (2000)
63. Ma, M., Ou, C., Wang, Z.A.: Stationary solutions of a volume-filling chemotaxis model with logistic growth and their stability. SIAM Journal on Applied Mathematics **72**(3), 740–766 (2012)
64. Ma, M., Wang, Z.A.: Global bifurcation and stability of steady states for a reaction-diffusion-chemotaxis model with volume-filling effect. Nonlinearity **28**(8), 2639 (2015)
65. Madzvamuse, A., Ndakwo, H., Barreira, R.: Cross-diffusion-driven instability for reaction-diffusion systems: analysis and simulations. Journal of Mathematical Biology **70**(4), 709–743 (2014)
66. Marik, C., Felts, P., Bauer, J., Lassmann, H., Smith, K.: Lesion genesis in a subset of patients with multiple sclerosis: A role for innate immunity? Brain **130**(11), 2800–2815 (2007)
67. Matkowsky, B.: Nonlinear dynamic stability. a formal theory. SIAM Journal on Applied Mathematics **18**(4), 872–883 (1970)
68. Meier, D., Guttmann, C.: MRI time series modeling of MS lesion development. NeuroImage **32**(2), 531–537 (2006)
69. Moghe, P., Nelson, R., Tranquillo, R.: Cytokine-stimulated chemotaxis of human neutrophils in a 3-D conjoined fibrin gel assay. Journal of Immunological Methods **180**(2), 193–211 (1995)
70. Mulone, G., Straughan, B.: Nonlinear stability for diffusion models in biology. SIAM Journal on Applied Mathematics **69**(6), 1739–1758 (2009)
71. Murray, J.D.: Mathematical Biology, vol. II. 3rd edn. Springer, New York (2007)
72. Nagaraja, S., Wallqvist, A., Reifman, J., Mitrophanov, A.: Computational approach to characterize causative factors and molecular indicators of chronic wound inflammation. Journal of Immunology **192**(4), 1824–1834 (2014)
73. Nimmerjahn, A., Kirchhoff, F., Helmchen, F.: Resting microglial cells are highly dynamic surveillants of brain parenchyma in vivo. Neuroforum **11**(3), 95–96 (2005)
74. van Noort, J., van den Elsen, P., van Horssen, J., Geurts, J., van der Valk, P., Amor, S.: Preactive multiple sclerosis lesions offer novel clues for neuroprotective therapeutic strategies. CNS and Neurological Disorders - Drug Targets **10**(1), 68–81 (2011)
75. Painter, K., Hillen, T.: Spatio-temporal chaos in a chemotaxis model. Physica D: Nonlinear Phenomena **240**(4-5), 363–375 (2011)
76. Peferoen, L., Vogel, D., Ummenthum, K., Breur, M., Heijnen, P., Gerritsen, W., Peferoen-Baert, R., Van Der Valk, P., Dijkstra, C., Amor, S.: Activation status of human microglia is dependent on lesion formation stage and remyelination in multiple sclerosis. Journal of Neuropathology and Experimental Neurology **74**(1), 48–63 (2015)
77. Penner, K., Ermentrout, B., Swigon, D.: Pattern formation in a model of acute inflammation. SIAM Journal on Applied Dynamical Systems **11**(2), 629–660 (2012)
78. Pennisi, M., Rajput, A.M., Toldo, L., Pappalardo, F.: Agent based modeling of treg-teff cross regulation in relapsing-remitting multiple sclerosis. BMC Bioinformatics **14**(16), S9 (2013)

79. Ponomarev, E., Shriver, L., Maresz, K., Dittel, B.: Microglial cell activation and proliferation precedes the onset of CNS autoimmunity. Journal of Neuroscience Research **81**(3), 374–389 (2005)
80. Popescu, B., Pirko, I., Lucchinetti, C.: Pathology of multiple sclerosis: Where do we stand? CONTINUUM Lifelong Learning in Neurology **19**(4), 901–921 (2013)
81. Quinlan, R., Straughan, B.: Decay bounds in a model for aggregation of microglia: application to Alzheimer's disease senile plaques. Proceedings of the Royal Society A: Mathematical, Physical and Engineering Sciences **461**(2061), 2887–2897 (2005)
82. Reynolds, A., Rubin, J., Clermont, G., Day, J., Vodovotz, Y., Bard Ermentrout, G.: A reduced mathematical model of the acute inflammatory response: I. Derivation of model and analysis of anti-inflammation. Journal of Theoretical Biology **242**(1), 220–236 (2006)
83. Rodríguez, N.: On the global well-posedness theory for a class of PDE models for criminal activity. Physica D: Nonlinear Phenomena **260**, 191–200 (2013)
84. Rodriguez, N., Bertozzi, A.: Local existence and uniqueness of solutions to a PDE model for criminal behavior. Mathematical Models and Methods in Applied Sciences **20**(SUPPL. 1), 1425–1457 (2010)
85. Ruiz-Baier, R., Tian, C.: Mathematical analysis and numerical simulation of pattern formation under cross-diffusion. Nonlinear Analysis: Real World Applications **14**(1), 601 – 612 (2013)
86. Sahraian, M., Radü, E.: MRI Atlas of MS Lesions. Springer-Verlag (2008)
87. Segel, L.A., Levin, S.A.: Application of nonlinear stability theory to the study of the effects of diffusion on predator-prey interactions. AIP Conference Proceedings **27**(1), 123–152 (1976)
88. Van Der Valk, P., Amor, S.: Preactive lesions in multiple sclerosis. Current Opinion in Neurology **22**(3), 207–213 (2009)
89. Wang, X., Xu, Q.: Spiky and transition layer steady states of chemotaxis systems via global bifurcation and Helly's compactness theorem. Journal of Mathematical Biology **66**(6), 1241–1266 (2013)
90. Wang, Z., Hillen, T.: Classical solutions and pattern formation for a volume filling chemotaxis model. Chaos **17**(3) (2007)
91. Wiendl, H., Hohlfeld, R.: Multiple sclerosis therapeutics: Unexpected outcomes clouding undisputed successes. Neurology **72**(11), 1008–1015 (2009)
92. Wollkind, D.J., Manoranjan, V., Zhang, L.: Weakly nonlinear stability analyses of prototype reaction-diffusion model equations. SIAM Review **36**(2), 176–214 (1994)
93. Wrzosek, D.: Global attractor for a chemotaxis model with prevention of overcrowding. Nonlinear Analysis, Theory, Methods and Applications **59**(8), 1293–1310 (2004)
94. Wrzosek, D.: Long-time behaviour of solutions to a chemotaxis model with volume-filling effect. Royal Society of Edinburgh - Proceedings A **136**(2), 431–444 (2006)
95. Wuerfel, J., Bellmann-Strobl, J., Brunecker, P., Aktas, O., McFarland, H., Villringer, A., Zipp, F.: Changes in cerebral perfusion precede plaque formation in multiple sclerosis: A longitudinal perfusion MRI study. Brain **127**(1), 111–119 (2004)
96. Zheng, J.: Boundedness of solutions to a quasilinear parabolic-elliptic Keller-Segel system with logistic source. Journal of Differential Equations **259**(1), 120–140 (2015)
97. Zheng, P., Mu, C., Hu, X.: Boundedness and blow-up for a chemotaxis system with generalized volume-filling effect and logistic source. Discrete and Continuous Dynamical Systems- Series A **35**(5), 2299–2323 (2015)